INTERNATIONAL JOURNAL OF HYDROGEN ENERGY 45 (2020) 23237–23253

Available online at www.sciencedirect.com

ScienceDirect

journal homepage: www.elsevier.com/locate/he

Sengon wood-derived RGO supported Fe-based electrocatalyst with stabilized graphitic N-bond for oxygen reduction reaction in acidic medium

Wulandhari Sudarsono [a], *Wai Yin Wong* [a,*], *Kee Shyuan Loh* [a], *Edy Herianto Majlan* [a], *Nirwan Syarif* [b], *Kuan-Ying Kok* [c], *Rozan Mohamad Yunus* [a], *Kean Long Lim* [a], *Ikutaro Hamada* [d]

[a] *Fuel Cell Institute, Universiti Kebangsaan Malaysia, 43600 UKM Bangi, Selangor, Malaysia*

[b] *Department of Chemistry, Universitas Sriwijaya, JI. Palembang-Prabumulih Km. 32 Inderalaya Sumsel 30662, Indonesia*

[c] *Malaysian Nuclear Agency, Bangi, 43000 Kajang, Selangor, Malaysia*

[d] *Department Precisions Science and Technology, Graduate School of Engineering, Osaka University, 2-1 Yamada-Oka, Suita, Osaka 565-0871, Japan*

HIGHLIGHTS

- RGO produced from biomass improved mass transport of oxygen.
- Improved ORR activity observed on Fe-Pani-RGO upon two-step pyrolysis.
- Graphitic N, Fe-Nx and mesopores contribute to improved ORR activity.

GRAPHICAL ABSTRACT

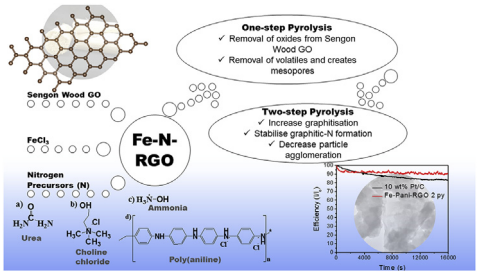

ARTICLE INFO

Article history:
Received 10 April 2020
Received in revised form
12 May 2020
Accepted 16 May 2020
Available online 30 July 2020

Keywords:
Fe–N-RGO
Catalyst support

ABSTRACT

This work reports utilised of RGO from Sengon wood biomass to support Fe–N–C noble-free catalyst (Fe–N-RGO), while also attempt to investigate the effect of pyrolysis stage on Fe–N-RGO catalysts with four different nitrogen precursors towards the ORR activity in acidic medium. One- and two-step pyrolysis were performed at 900 °C for 1 h and 2 h respectively to produce Fe–N-RGO. This work revealed that two-step pyrolysis was able to remove the volatile components and hence forming more graphitised, stable graphitic-N and Fe-Nx, synergistically improve the ORR activity with highest onset potential of 0.83 V vs RHE and limiting current density of 5.33 mA cm^{-2} reported on Fe-Pani-RGO 2py. An increase in the kinetic on Fe-Pani-RGO 2py with Tafel slope of 74 mV/dec operated at

* *Corresponding author.*
E-mail addresses: waiyin.wong@ukm.edu.my, waiyin.wwy@gmail.com (W.Y. Wong).
https://doi.org/10.1016/j.ijhydene.2020.05.158

Acidic medium
Oxygen reduction reaction

80 °C was reported. The mesoporous structure on RGO increases the stability by 8% and better methanol tolerance when compared to a benchmark Pt/C catalyst.

Introduction

Polymer exchange membrane fuel cells (PEMFCs) can be ideally used for generating portable electricity; furthermore, they do not produce pollutants, are easy to maintain and have a high energy efficiency. The electrochemical reaction involved in generating electricity is based on the oxidation of hydrogen and reduction of oxygen in the Polymer exchange membrane fuel cells (PEMFC) system. On the cathode side, the oxygen reduction reaction (ORR) shows sluggish kinetics, which affects the overall performance of the fuel cell. An increase in the catalyst loading of a state-of-the-art Pt/C catalyst on the cathode is the current solution for resolving this issue without compromising the manufacturing cost.

To overcome this, first-row transition metals, called non-precious metal (NPM) catalysts, have gained considerable attention owing to their ability to catalyse reactions and their increased abundance. With the use of pyrolysis, the production of NPMs with various forms of catalyst precursors, such as chalcogenides [1], metal organic frameworks [2], bimetallic compounds with carbon precursors [3], metal-based enzymes [4] and metal salts with polymeric nitrogen precursors (Me–N–C) [5,6], has been extensively examined for use as ORR electrocatalysts. Among the various forms listed above, pyrolysed Me–N–C has gained the most attention owing to its facile synthesis, cost effectiveness, environmental friendliness and good performance as an ORR catalyst [7–9].

Presently, Me–N–C-based catalysts have been shown to exhibit high ORR activities that are similar or even superior to a benchmark Pt/C catalyst in alkaline media. The incorporation of first row transition metal such as Fe or Co, heteroatom and carbon support has synergistically formed the active sites of Me-N_x for ORR, which has been shown to have increase the catalytic activity [10,11]. Among most of the reported Me–N–C electrocatalyst, Fe–N–C based catalysts have demonstrated its high ORR activity as well as single cell performance in both acidic and alkaline electrolyte attributed to the sufficient binding energy for oxygen adsorption on the surface of Fe-N_x [12–14].

However, in long term acidic PEMFC environment, NPMs often suffer from a high rate of metal dissolution and carbon oxidation. Various efforts have been made, such as the encapsulation of transition metals (Fe, Co, and Ni) into carbon nanoshells [15,16] and the addition of polymeric material to a catalyst, particularly Fe-PPy/Pani (polypyrrole/polyaniline)-C [17], to create stable active sites in acidic environments. Highly graphitic porous carbon such as carbon nanotubes, Vulcan carbon, graphite and graphene have been reported to be used as supports in ORR catalysts and have been shown to improve the durability and activity of catalysts. This is attributed to highly graphitic porous carbon having a large surface area, high porosity and resistance to oxidation in acidic media [18–20].

Recently, numerous works have focused on investigating the properties of more sustainable, environmentally friendly and low-cost porous carbon sources, namely, biomass carbon that is derived from cellulosic wood [21–23]. The biomass carbon is beneficial because of its unique morphology and the presence of impurities, and because it serves as a porous catalyst support with high surface area and defect sites on the surface. There have been some works that have employed biomass sources as catalyst supports, such as Feculae Bombycis (FC) [24], brewer's yeast [25], and soybean [26]. Among the biomass carbon-based catalysts, Fe doped with FC has been reported to be a dual-function catalyst in alkaline and acidic media. Meng et al. [24] reported that an Fe–C catalyst with a hierarchical porous carbon support derived from FC exhibited an ORR onset potential of 0.92 V vs RHE, a half wave ($E_{1/2}$) of 0.81 V in 0.1 M KOH, and a low ORR activity with an onset potential of 0.7 V vs RHE and a half wave of $E_{1/2} = 0.6$ V in 0.5 M H_2SO_4. Interestingly, biomass has also shown its potential to be converted into a graphene-like structure, which is among the most stable carbon-based support for the catalyst. For instance, woody biomass, such as spruce bark and populous wood, have been reported to have successfully converted into a few-layer graphene-like structures with specific surface areas of 2385 m^2/g and 1317.1 m^2/g, respectively [21,27]. The ability of the woody biomass to be converted into graphene-like structure is believed to be attributed by multilayer porous network formed by cellulosic component. These works has inspired more efforts to utilize woody biomass as a support for metal- and heteroatom-doped catalysts. For application as catalyst support, it is seen beneficial with the presence of impurities in the biomass itself. Upon chemical and heat treatment, the removal of the impurities on the surface of carbon can result in the formation of surface defect, which can be served as a strong anchoring site for the catalyst [28–30]. Whilst, base activation and mechanical exfoliation process are commonly reported in literature to convert the biomass into graphene-like structure [27,31].

Interestingly, an agricultural cellulosic woody biomass, called Sengon wood, originates from Indonesia was shown to exhibit a hierarchical porous bulky morphology (refer to Fig. S1). which was found to be able to form multilayer mesoporous carbon structure after pyrolysis [32]. We have reported in our previous work that through Hummer's method, the Sengon wood has been successfully converted into reduced graphene oxide (RGO) which was shown to be able to exhibit similar characteristics as the RGO produced from graphite through the same method [33]. The presence of a highly defective surface, after the removal of impurities during the treatment process to produce biomass RGO, provides

an opportunity to create a dual-function catalyst for ORR in acidic environments; for instance, the biomass RGO can serve as both the Fe–N–C catalyst support for oxygen reduction reaction and a metal-protecting shell, as reported in our previous works [33,34].

In the process of catalysing ORR in an acidic medium, noble-metal-free catalysts are expected to have high surface area, active catalytic sites such as Fe-N_x, and a high degree of graphitisation, thereby enhancing the reactant mass transport and improving electron transfer [35]. Pyrolysis technique has been observed to be a convenient method for producing well-distributed particles and the desired Fe-N_x sites that are necessary for influencing ORR activity [36]. Our previous work demonstrated that the Fe–N-RGO produced via a one-step pyrolysis exhibited superior ORR performance in alkaline media. In this work, we attempt to study a noble-metal-free catalyst with a Sengon wood-derived RGO support for the ORR under acidic media (0.1 M $HClO_4$). The GO precursors from a Sengon wood are prepared through the conventional Hummer's method as reported in our recent work [33]. Noting that the morphology and chemical bonding show a significant effect on the ORR activity, especially in acidic media, we focus on the effect of one-step and two-step pyrolysis methods on the ORR activity and stability of the noble-metal-free catalyst.

Experimental section

Fe–N-RGO catalyst preparation

The preparation procedure of GO from Sengon wood and of the Fe–N-RGO catalyst followed our previous work [24]. In this work, four different nitrogen precursors (denoted as N) were investigated to produce Fe–N-RGO, (N = Urea, Ammonia, Choline Chloride (ChoCl) and Polyaniline (Pani)). For Fe-Ammonia-RGO preparation, 2 mmol of $FeCl_3$ (Systerm, ChemPur) and 149.2 μL of ammonia solution (Systerm ChemAr, 37%) were magnetically stirred along with GO powder (Fe:C ratio is 2:5 by mass). A hydrothermal process was employed with the mixture was subjected to operating temperature of 190 °C for 8 h and was followed by oven drying at 80 °C to obtain the sample powder. To investigate the effect of one-step and two-step pyrolysis on the Fe–N-RGO samples, the following procedures were conducted. For the one-step pyrolysis, dry powder from each Fe–N-RGO was collected, and all catalysts were subjected to pyrolysis in a tube furnace at a fixed temperature of 900 °C under a continuous flow of nitrogen gas for 1 h. After cooling, the obtained catalyst was washed with 0.5 M H_2SO_4 for 6 h and then was rinsed with deionised water. The slurry was dried overnight at 80 °C. For the two-step pyrolysis, the obtained samples were subjected to a second pyrolysis at the same temperature for 2 h.

Physicochemical characterization

Field emission scanning electron microscopy (Carl Zeiss Gemini SEM 500) measurement was conducted with secondary electron scattering at 15 kV and a magnification of 20,000 ×. X-ray diffraction (XRD, PANalytical X'Pert Pro MPD PW 3040/60) measurement was conducted by scanning at a wide angle of $2\theta = 10°–80°$ with a scan rate of $2° \text{ min}^{-1}$. Raman spectroscopy (Thermo Scientific, DXR2xi) measurement was conducted using a 532-nm confocal laser detector at 10 kV. Transmission electron microscopy (TEM) and selective area electron diffraction (SAED) analyses were conducted on a Thermo Fisher Talos 120C with magnifications of 310 k and 650 k and an accelerating voltage of 120 kV. A Micromeritic 3 Flex device was used to measure the surface area via the Brunauer-Emmett-Teller (BET) method, and the pore size distribution was predicted by the Barrett-Joyner-Halenda (BJH) and NLDFT methods. X-ray photoelectron spectroscopy (XPS, Synchotron Beamline 3.2Ua) experiment was conducted with wide scan (0–900 kV) and narrow scan (Fe and N) deconvolutions to investigate the type of bonding that occurred in the catalyst system. In the surface scan, the total elemental composition (wt. %) was calculated based on the convergence of the peak area of each element on the binding energy range of the reference, with r.s.f = 1. The types of elemental bonding were investigated in the narrow scan and presented as atomic percentage (at%).

Electrochemical testing

A glassy carbon electrode (GCE) with a surface area of 0.1962 cm^2 was employed to deposit 400 μg^{-2} of the Fe–N-RGO catalyst ink onto it. Prior to catalyst ink deposition, the glassy carbon electrode was polished with 0.05 μm size alumina slurry into a transparent mirror-like surface. Meanwhile the measurement cell with 50 mL volume was soaked with the electrolyte overnight prior to ensure no impurities present in the electrolyte. Stationary tests were conducted via cyclic voltammetry (CV); meanwhile hydrodynamic tests were performed electrochemically using a rotating ring disk electrode (RRDE, Gamry) on the Autolab PGSTAT128N potentiostat. A three-electrode system was used to study the oxygen reduction reaction in a half cell environment. The GCE with a platinum ring (Pine Instrument) was the working electrode, Pt wire (Metrohm) and 3 M Ag/AgCl (Metrohm) were the counter electrode and reference electrode, respectively. For cyclic voltammetry measurement, a wider potential window of −0.2 to 1.2 V vs Ag/AgCl ($E_{RHE} = E_{Ag/AgCl} + 0.2885$ V) at a rate of 10 mV s^{-1} was used to study the redox reactions of Fe–N-RGO catalysts under the N_2 and O_2 environment in 0.1M $HClO_4$ and thus to determine the oxygen reduction potentials of the catalyst [37]. Meanwhile, based on the potential range for oxygen reduction that occurs on the catalyst from CV, a narrower potential window of 0.1–0.9 V vs Ag/AgCl was used to study specifically on the kinetic aspects of the catalysts through linear sweep voltammetry (LSV) on the RRDE system. Different rotation speed of 400–1600 rpm were used for the LSV study.

The electron transfer number (n) obtained from the LSV was compared via two methods, i.e. Koutechy-Levich (K-L) plot and current densities obtained on the disk (I_d) and ring (I_r) using the RRDE system. A K-L plot was obtained from the LSV curve in a mixed-kinetic controlled region of 0.4–0.6 V vs RHE. The slope from the rotation speed (ω) versus current density (I) curve was extracted and written as Eq. (1).

$$\frac{1}{I} = \frac{1}{I_k} + \frac{1}{I_l} = \frac{1}{I_k} + \frac{1}{0.62nFAC_o^* D_o^{2/3} \upsilon^{-1/6} \omega^{1/2}} \quad (1)$$

where Faraday number, $F = 96{,}485$ °C mol^{-1}; kinematic viscosity, $\upsilon = 0.01$ cm^2 s^{-1}; diffusion coefficient of O_2 in electrolyte, $D_o = 1.67 \times 10^{-5}$ cm^2 s^{-1}; and O_2 bulk concentration, $C_o = 1.38 \times 10^{-6}$ mol cm^{-3} [38].

Eq. (2) is used to calculate n, with the ring collection efficiency of 0.26. Meanwhile, the percentage of peroxide production from the oxygen reduction process is obtained through Eq. (3).

$$n = \frac{4I_d}{I_d + \frac{I_r}{N}} \quad (2)$$

$$\% \text{ of } HO_2^- = \frac{4-n}{2} \times 100\% \quad (3)$$

Further kinetic analysis was performed on the catalysts on both the low current density range of 1.15–1.05 V vs RHE and a high current density of 0.8–0.7 V vs RHE by plotting the log i_k vs potential (V vs RHE) extracted from the LSV curve. The analysis involved the values of the thermodynamic overpotential (η, V), Tafel slope (b, mV dec^{-1}), transfer coefficient (α) and exchange current density (i_o, mA cm^{-2}) at elevated temperatures of 25–80 °C. The Butler-Volmer equation was employed, which is written as Eq. (4).

$$\eta = a \log i_o - b \log i_k \quad (4)$$

and the Tafel slope was calculated using Eq. (5).

$$b = -\frac{2.303\,RT}{\propto nF} \quad (5)$$

where R is the gas constant (8.314 J K^{-1} mol^{-1}), T is the operating temperature (K) and F is Faraday's constant (96,485 C mol^{-1}).

The durability and methanol tolerance were determined using chronoamperometry with a rotation speed of 1600 rpm in an O_2 environment. For the durability test, the catalyst response to a decrease in the current density was measured over 16, 000 s by applying a potential of 0.53 V to the RRDE system. Moreover, for the methanol tolerance, 6 mL of methanol was injected into the system after running for 200 s, and the percentage of the decrease in current density over the initial value (I/I_o) before the methanol addition was calculated as the methanol tolerance of the catalyst.

Result and discussion

Effect of the one-step and two-step pyrolysis processes on the physicochemical and ORR activity of the Fe–N-RGO catalyst

Fig. 1(a) shows the TEM micrograph of the Sengon wood-derived RGO produced through the Hummer's method and pyrolysis at 900 °C. The transparent nanosheet structure was clearly observed with a lattice fringe, as observed in Fig. 1(b); moreover, the SAED image in the inset of Fig. 1(b) features a dotted spot ring, indicating the presence of a crystalline structure. These observations confirm the formation of a multilayer graphene structure produced from Sengon wood [39–41]. The RGO produced through this method is used as the support for the Fe–N–C catalyst, which is further denoted as Fe–N-RGO (where N = Urea, Ammonia, ChoCl or Pani). The FESEM micrographs in Fig. 1(c–j) shows the morphological changes of the Fe–N-RGO catalysts after the one-step and two-step pyrolysis processes.

For both the Fe-Urea-RGO (Fig. 1(c, d)) and Fe-Ammonia-RGO (Fig. 1(e, f)) catalysts, they demonstrate similar morphology transformations. The one-step pyrolysis produces coarse and dense structures, indicating the aggregation of catalyst particles [42]. In contrast, the two-step pyrolysis removes some volatiles and therefore forms a more graphitic and less dense structure, which appears to be crumpled. It is also worth noting that RGO appears as a sheet-like structure that retains its morphology after the addition of the iron-nitrogen-based catalyst. It is suggested that the crumpled structure is induced by the aggregation of iron oxide particles during the stirring process, and the subsequent pyrolysis process incorporates the N and Fe particles on the RGO matrix [36].

Nitrogen salt is suggested to covalently bond on RGO, while Fe physically anchors on the edge and basal planes of RGO [43]. Moreover, Fe-ChoCl-RGO (Fig. 1(g, h)) depicts a similar sheet-like structure after the one-step and two-step pyrolysis processes. The homogenous flat sheet structure infers the presence of a graphene-like structure from the Sengon wood RGO and ChoCl. $FeCl_3$ is a type II eutectic solvent [44] and according to Mondal et al. [45], deep eutectic solvents act as soft templates for the growth of graphene nanosheet structures. Hence, it is speculated that the presence of a deep eutectic solvent has assisted the formation of the flat sheets with the incorporation of Fe and N into the base matrix of RGO. Interestingly, when using the Pani polymer as a nitrogen source, Fe-Pani-RGO 1 py (Fig. 1(i)) shows dense interconnected tubular spheres after the one-step pyrolysis. Furthermore, Fe-Pani-RGO 2 py shows the most vivid structural transformation after the second-step pyrolysis and forms a less dense sheet structure (Fig. 1j) [46]. Pyrolysis applies excessive energy on the polymer and induces a self-assembled sheet structure on the surface [47]. These less dense sheet structures can benefit from a fast and less energetic distribution of mass transport on the catalyst surface [48,49].

Fig. 2(a & b) shows the XRD pattern of the Fe–N-RGO catalysts produced from the one-step and two-step pyrolysis processes, respectively. The XRD patterns of Fe-Pani-RGO 1 py and Fe-ChoCl-RGO 1 py in Fig. 2(a) display two prominent peaks at 2θ of 26° and 44°, which is ascribed to the predominance of the disordered graphitic carbon phase of RGO [27,50]. At 2θ = 26°, Fe-Pani-RGO displays a rather broad peak compared to that for Fe-Urea-RGO and Fe-Ammonia-RGO, which is ascribed to the overlapping interface between the Pani and few-layer RGO [51]; moreover, the sharp peak in Fe-ChoCl-RGO infers the high crystallinity and well-ordered restacking on RGO due to the presence of the deep eutectic solvent and Fe particles [52]. It should be noted that at 2θ = 44°, iron carbide (Fe_3C) may overlap with the dominant N-RGO peak and be less accessible for defining the molecular phase

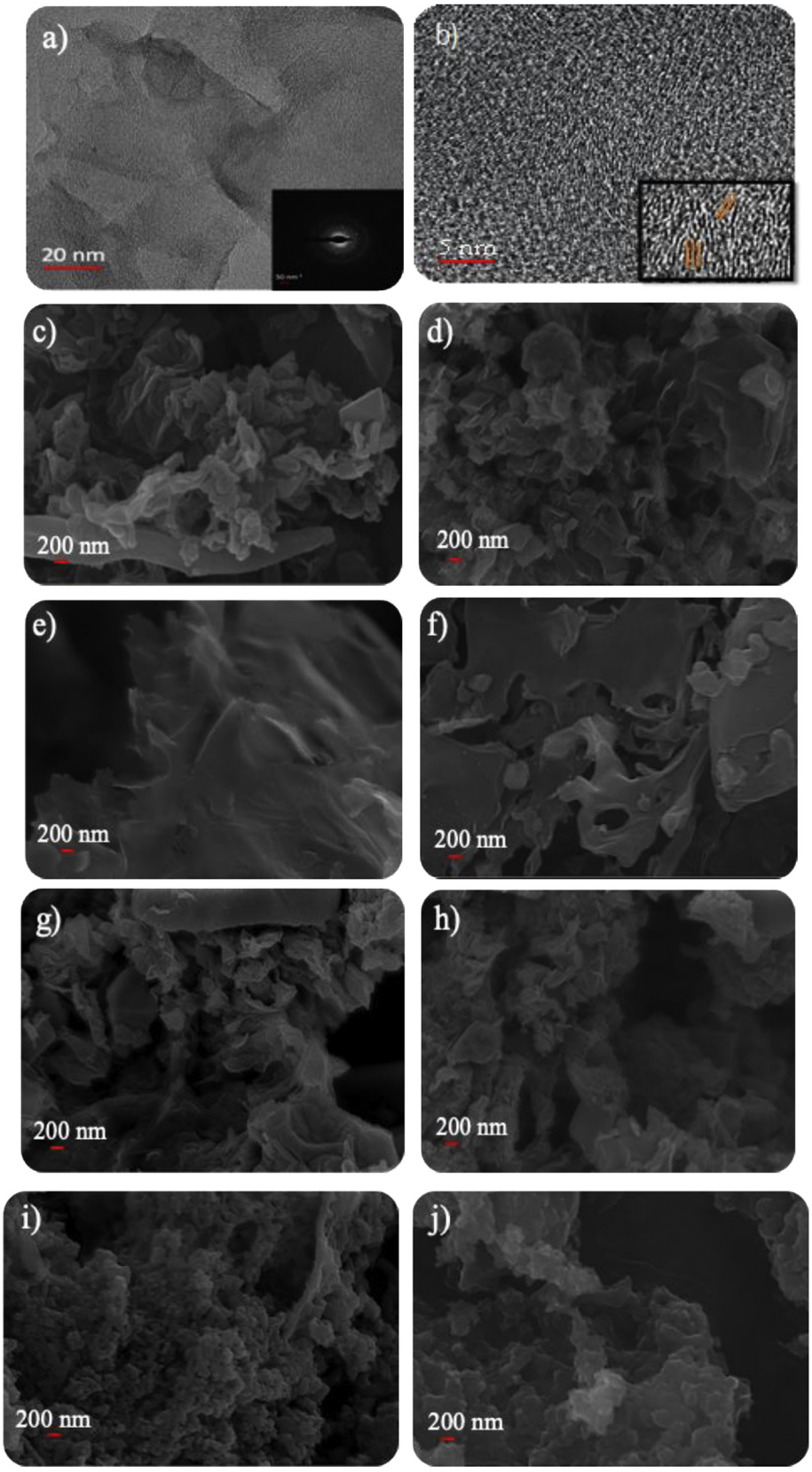

Fig. 1 – (a) TEM and (b) HRTEM images of RGO (inset showing lattice fringe), respectively. FESEM images of (c), (d) Fe-Urea-RGO 1 py and 2 py (e), (f) Fe-Ammonia-RGO 1 py and 2 py (g), (h) Fe-ChoCl-RGO 1 py and 2 py, and (i), (j) Fe-Pani-RGO 1 py and 2 py.

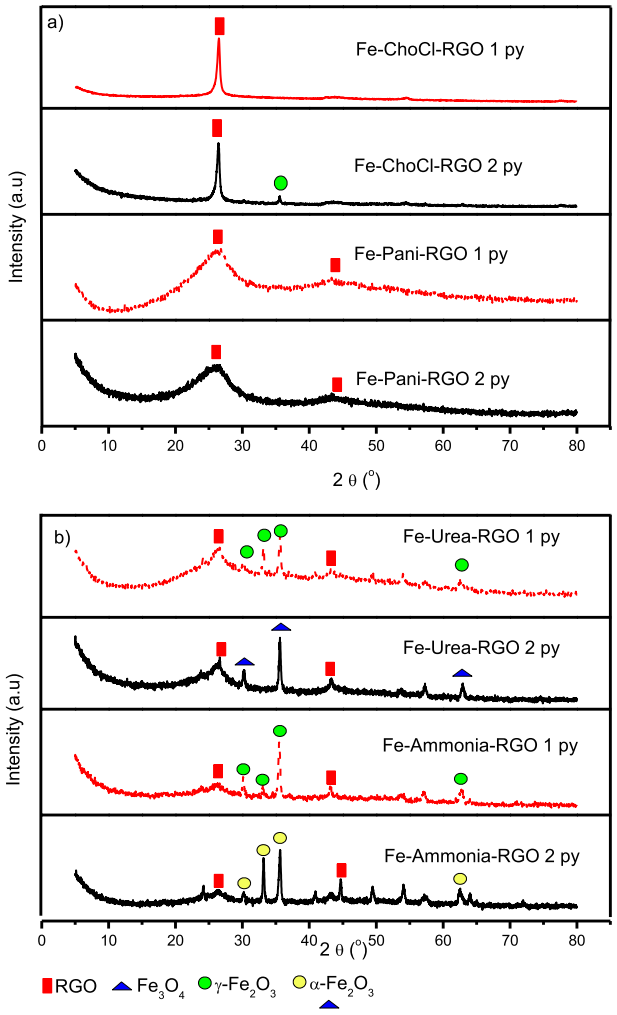

Fig. 2 – X-Ray diffraction peaks of (a) Fe-ChoCl-RGO 1 py and 2py; Fe-Pani-RGO 1 py and 2 py and (b) Fe-Urea-RGO 1 py and 2 py; Fe-Ammonia-RGO 1 and 2 py.

[53]. After the second step pyrolysis, an increase in the graphitic structure was demonstrated by the higher peak intensity at $2\theta = 26°$ for both Fe-ChoCl-RGO 2 py and Fe-Pani-RGO 2 py samples. The visible higher crystallinity corresponds to the less agglomerated structure that can be observed by the FESEM images, which defined a more ordered graphitic structure formation [54].

Similar to Fe-Pani-RGO and Fe-ChoCl-RGO, the existence of the peaks at 26° and 44° infer the existence of RGO sheets on the Fe-Urea-RGO and Fe-Ammonia-RGO samples, as demonstrated in Fig. 2(b). Moreover, the sharp peaks observed at $2\theta = 24.1°$, 34°, 35.6°, 53.8° and 63° for Fe-Urea-RGO 1 py are assigned to the Fe_2O_3 phase in accordance with ICDD No. 00-016-0653. After the second pyrolysis step, the peak at $2\theta = 34°$ disappeared, indicating the transformation of Fe_2O_3 into Fe_3O_4 (ICSD 98-002-2141) [55].

On the other hand, Fe-Ammonia-RGO shows the existence of Fe_2O_3 for both the one-step and two-step pyrolysis processes whereby after the two-step pyrolysis, the iron oxide is transformed from γ- Fe_2O_3 into α- Fe_2O_3 [56]. This implies that the Fe-phase anchored on Fe-Ammonia-RGO is thermally stable. Interestingly, after the two-step pyrolysis process, Fe-Ammonia-RGO displays the presence of an Fe–N phase at $2\theta = 30°$, 49°, 61° and 62°. The similar change in the Fe phase for Fe-Urea-RGO and Fe-Ammonia-RGO is also consistent with the similar morphology obtained for both samples after the one-step and two-step pyrolysis processes. The two-step pyrolysis evaporates some volatiles and impurities on the nanostructure and promotes the predominant growth of more stable graphitic and crystalline sites on the catalyst.

Herein, Raman spectroscopy was used to study the effect of the two-step pyrolysis process towards the degree of graphitisation due to Fe-Pani-RGO 1 py and 2 py having the greatest morphological change in their structure. The Raman spectra show peak intensities at ~1345 cm^{-1}, which is assigned to the carbon disorder peak, D band, and at ~1583 cm^{-1}, which is assigned to the sp^2 carbon graphitic peaks, G band (refer to Fig. S2 for detail). Furthermore, the I_D/I_G ratio is calculated to compare the degree of defective sites on the catalyst surfaces, which then reflects the degree of graphitisation. Upon thermal treatment, nitrogen and iron are anchored to the RGO surfaces and generate additional active sites, which is proven by the higher I_D/I_G ratio (1.04 and 1.07 for Fe-Pani-RGO 2 py and Fe-Pani-RGO 1 py) when compared to RGO 900 ($I_D/I_G = 0.92$). Nonetheless, a two-step pyrolysis treatment induces a decrease in defective sites on the catalyst and is assigned to an increase in the graphitic structure of the catalyst [57]. These results are in good agreement with the FESEM results that display a more ordered sheet structure. The high degree of graphitisation is beneficial for further increasing the mass transfer during ORR [14,58].

Aside from the morphology and crystallinity, the elemental (Fe and N) contents of the samples were carefully observed via XPS to reveal their correlation with ORR activity. In Fig. 3(a & b), the scan for both the one-step and two-step pyrolysis processes in the range of 0–900 eV show the existence of Fe, N, O and C. The high carbon content is attributed to the presence of RGO in the Fe–N-RGO compounds. A major decrease in O was observed after the second pyrolysis, which is attributed to the removal of oxides from the Fe–N-RGO. It is obvious that Fe has an inconsistent trend after pyrolysis due to the low attenuation of its metallic bond lengths, which are less sensitive to XPS characterization [59].

From the structural morphology, it is suggested that nitrogen sources will covalently bond on RGO, while Fe will physically anchor on the edge and basal planes of RGO [60]. Both atoms act as major sites where the reactants, intermediates, protons and electrons are involved in the electrochemical reaction. To reveal the nature of the catalytic active sites, the Fe and N peaks are observed in a narrow scan. The bonding nature of Fe is deconvoluted in a range of 707–730 eV (Table 1), where each peak represents a species of iron with oxidation states of Fe^0, Fe^{2+} or Fe^{3+}. At 710 ± 2 eV, Fe^{2+} is implied for the formation of FeO, $Fe(OH)_2$ and iron-nitrogen bonds, such as Fe-N_x species [61], which are predominant in Fe-Pani-RGO, as shown in Table 3. Besides, less defined satellite peaks at 719 eV also assigned for low concentration of Fe oxides form [62,63]. Fe species play a role on improve the electron transfer; thus, an increase in Fe content after the two-step pyrolysis will slightly increase the onset potential [64].

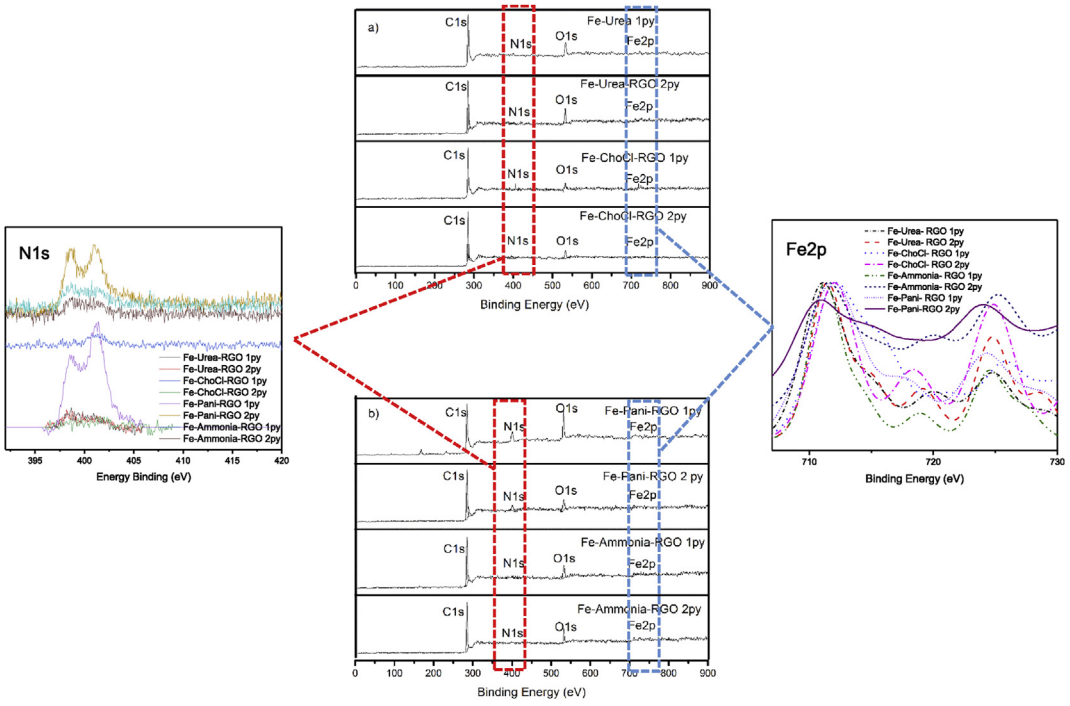

Fig. 3 – XPS of (a) Fe-ChoCl-RGO 1 py and 2py; Fe-Pani-RGO 1 and 2 py and (b) Fe-Urea-RGO 1 and 2 py; Fe-Ammonia-RGO 1 and 2 py. Inset shows the narrow scans of N 1s and Fe 2p. Percentages for the N deconvolution peaks after (c) one-step and (d) two-step pyrolysis.

In addition to Fe, the nature of N bonding is analysed, as it is believed that the presence of nitrogen has a positive contribution to the ORR activity. The N peaks are deconvoluted into 4 type bonding at range of 396–406 eV, with respect to the following; e.g: pyridinic N at 398.3 ± 2 eV, pyrrolic N 400.4 ± 2 eV, graphitic N 401.5 ± 2 eV, and oxidized N 403.2 ± 2 eV (see Table S1 and Fig. S3). As depicted in Fig. 3(c & d), the polymeric sources such as Pani gained the highest N content due to their high molecular density, while other salt sources contained lower N at.%. The one-step pyrolysis demonstrates the major existence of pyridinic and graphitic N and therefore emphasizes the distribution of nitrogen bonding on the edge and basal planes of the catalyst. These N bonds synergistically catalyse the ORR by lowering the activation barrier of the intermediates during the O_2 reduction process and increase the rate of catalytic reaction on the cathode [65,66].

Nonetheless, the intensity of the N atom decreases significantly after the two-step pyrolysis due to the breakage of some volatile N bonds at high temperature. Interestingly, Fe-ChoCl-RGO 2 py, Fe-Pani-RGO 2 py, and Fe-Ammonia-RGO 2 py retain their graphitic N percentages despite a decrease in their N content. This signifies the high chemical stability of graphitic N at high temperature, and it has been suggested that the presence of sp^2 lone pairs on the graphitic basal plane is the cause for the increase in electron transfer [67].

Regarding the specific surface area and pore size, a BET adsorption and desorption analysis was conducted, and isotherms were obtained for the sample with the highest nitrogen content (Fe-Pani-RGO, refer to Fig. S4). The linear isotherm plot of each Fe-Pani-RGO shows a similar trend and is specific to a type IV isotherm and type III open hysteresis loops at a high relative pressure ($p/p_o > 0.5$). The isotherm plot is consistent with a crumpled and dense structural morphology that is assigned to the growth of aggregated macropore/mesopore voids instead of micropores [68]. Mesopores are more favourable for generating a well-distributed mass transport of reactant during catalytic activity [62], and it is apparent that two-step pyrolysis increases this characteristic. A large hysteresis loop and surface area, as represented by Fe-Pani-RGO 2 py (29.2 m^2g^{-1}) compared to Fe-Pani-RGO 1 py (19.58 m^2g^{-1}), is due to an increase of the unclogged cavities of the pore structure [69]. It should be noted that two step pyrolysis decreased the BJH pore size from 29.0 nm to 21.2 nm after the second pyrolysis (Table 2). This finding is in good agreement with the morphology characterization that shows a less dense structure after the two-step pyrolysis treatment.

Based on the physicochemical characterization, it is observed that the pyrolysis treatment is crucial in promoting the growth of active sites on the catalyst surface [70]. It can be concluded that the following structural transformation takes place after the one-step and two-step pyrolysis processes. In the first step of pyrolysis (at 900 °C for 1 h under a N_2 flow), the oxygen functional groups on graphene oxide are removed, thus initiating the creation of pores on the catalyst through the volatilisation of organic compounds [71]. Upon second step pyrolysis, in which the catalyst samples were subjected to prolonged heat treatment, it was observed with the reduction in the nitrogen content and increase in graphitic N composition, increase in the crystallinity and porosity as well as the formation of less agglomerated structure. These findings lead to our believe that the second step pyrolysis has indeed further

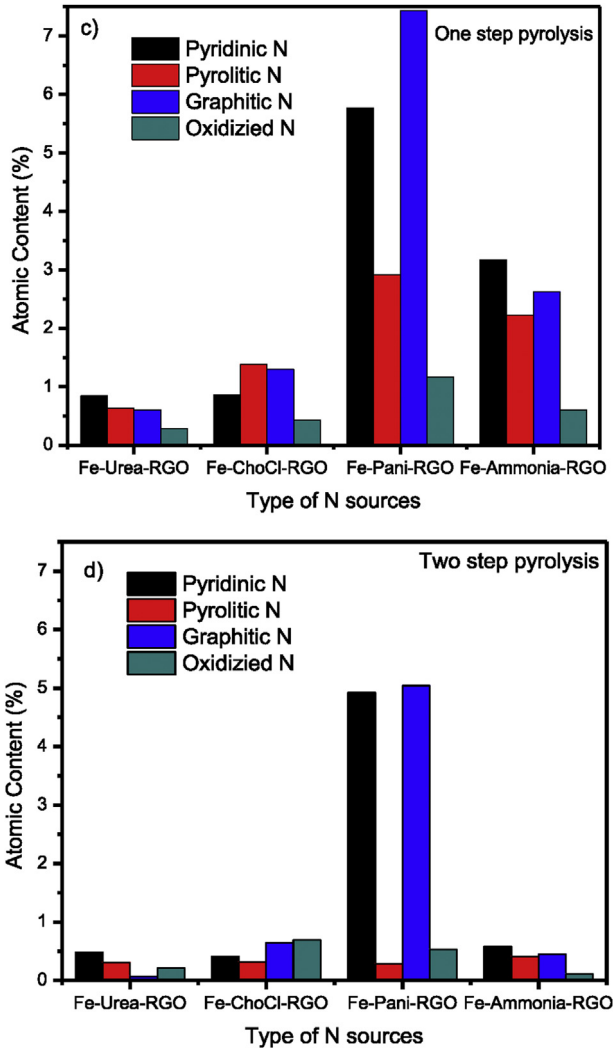

Fig. 3 – *(continued)*.

removed unstable or volatile components remained on the catalyst structure, allowing the restructuring of the catalyst into more porous and stable form, resulted in the increase in graphitisation degree and graphitic-N which is more dominant in catalyst pyrolysed at higher temperature [72,73].

Table 2 – Surface area of Fe-Pani RGO 1 py and 2 py along with that of Fe-Pani-RGO Gr.

	Fe-Pani-RGO 1 py	Fe-Pani-RGO 2 py	Fe-Pani-RGO Gr
BET Surface Area	19.58 m^2g^{-1}	29.20 m^2g^{-1}	18.9 m^2g^{-1}
External surface area	17.47 m^2g^{-1}	26.70 m^2g^{-1}	17.89 m^2g^{-1}
BJH adsorption pore size	29 nm	21.2 nm	28.2 nm
Total volume pores	0.081 cm^3g^{-1}	0.082 cm^3g^{-1}	0.087 cm^3g^{-1}

The electrochemical performance was investigated via CV and linear sweep voltammetry (LSV) in a 0.1 M $HClO_4$ electrolyte in an O_2 and N_2 environment. In the first attempt, static mass transfer is conducted via CV, where the CV curve qualitatively describes the catalytic activity. The redox peaks of Fe^{2+}/Fe^{3+} appear at approximately 0.62 V vs RHE as an anodic peak and approximately 0.83 V vs RHE as a cathodic peak in the inert N_2 environment (refer to Fig. S5). The above observations implies that the catalysts show pseudocapacitance behaviour due to the successful incorporation of iron metal on the RGO lattice [18]. The large area of the background curves inferred to large capacitance of the catalyst, which is caused by large pores on the surface and is beneficial for preserving durability under acidic conditions.

Furthermore, in the O_2 potential window as depicted in Fig. 4(a), each catalyst showed different onset potentials and reduction peaks in the CV curves, depending on the nature of the N sources and the step of pyrolysis. The low current density observed on the Fe-Pani-RGO 1 py sample indicates its inferior activity, which is caused by the inhomogeneity of the agglomerated structure. In addition, the Fe-ChoCl-RGO 1 py that is tuned into a thin sheet morphology shows a high onset potential of 0.76 V vs RHE. The pyrolysis step has been shown to redistribute the nitrogen bonding and content on the surface of the carbon matrix while improving the graphitic structure [74], as seen by the wide voltammograms of Fe-Pani-RGO 2 py and Fe-ChoCl-RGO 2 py. A well-defined reduction peak is expressed by Fe-Pani-RGO 2 py with an onset potential of 0.8 V vs RHE and a reduction peak of 0.45 V vs RHE. Thus, Fe-Pani-RGO 2 py is shown to have the highest ORR activity after a redox correction in a N_2 environment.

Table 1 – Elemental composition (at.%) of Fe–N-RGO through XPS analysis.

Samples	Fe2p (wt.%)	N1s (wt.%)	O1s (wt.%)	C1s (wt.%)	Atomic content (at.%)				
					$Fe^{2+}{}_{3/2}$	$Fe^{2+}{}_{1/2}$	satellite peaks	$Fe^{3+}{}_{3/2}$	$Fe^{3+}{}_{1/2}$
One-step pyrolysis									
Fe-Urea-RGO 1 py	2.39	2.36	23.37	71.89	1.08	0.35	0.32	0.46	0.18
Fe-ChoCl-RGO 1 py	4.86	3.97	11.53	79.64	1.8	1.05	0.49	0.88	0.64
Fe-Pani-RGO 1 py	1.41	17.29	30.69	50.62	0.27	0.43	0.22	0.33	0.16
Fe-Ammonia-RGO 1 py	6.41	8.625	26.91	58.05	3.13	0.82	0.53	1.36	0.58
Two-step pyrolysis									
Fe-Urea-RGO 2 py	4.252	1.062	22.29	72.4	1.60	0.61	0.52	1.06	0.46
Fe-ChoCl-RGO 2 py	6.179	2.065	23.37	68.39	1.99	0.30	1.01	1.98	0.89
Fe-Pani-RGO 2 py	4.21	10.77	22.63	62.4	1.88	0.75	0.25	1.03	0.29
Fe-Ammonia-RGO 2 py	4.18	1.54	21.37	72.91	1.78	0.48	0.54	1.01	0.38

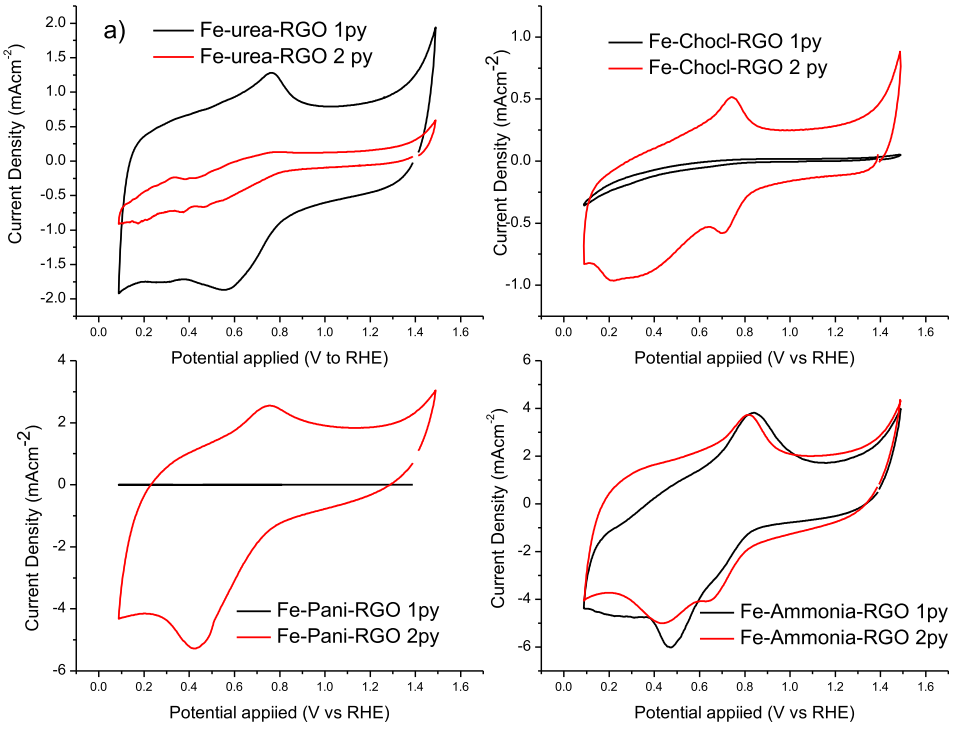

Fig. 4 – a) Cyclic voltammetry (CV) and linear sweep voltammetry for the b) one-step and c) two-step pyrolysis processes of Fe-Urea-RGO, Fe-ChoCl-RGO, Fe-Pani- RGO, and Fe-Ammonia-RGO at 1600 rpm under saturated O_2 conditions of 0.1 M $HClO_4$.

Fe-Ammonia-RGO 1 py and 2 py show analogous reduction peaks at 0.48 V, with pair of $Fe^{2+/}Fe^{3+}$ redox peaks at 0.66 V and 0.8 V, which is consistent with minor changes in morphology and crystallinity between one- and two-step pyrolysis. Obviously, the pyrolysis step exerts a negative influence on Fe-Urea-RGO, whereby the reduction peak shifts negatively by 12 mV after 2 py. This is correlated to an iron oxide transformation that is less favourable for ORR activity.

A dynamic mass transfer is observed through the RRDE method at a high rotation rate of 1600 rpm, in attempt to achieve a mass transfer-free region. The results of the Fe–N-RGO sample are identified in a potential range of 0.2–1.0 V vs RHE under saturated O_2 conditions and are subsequently presented after background correction. As shown in Fig. 4(b) and Table 3, the LSV graph shows an onset potential in the range of 0.7–0.8 V vs RHE, and a half wave potential ($\Delta E_{1/2}$) of 0.6–0.7 V vs RHE. Again, Fe-Pani- RGO 1 py, displays an inferior onset and half wave potential compared to those from other sources. This is attributed to the poor distribution of active sites and less porous structure, which is in good agreement with the BET surface area and FESEM results [75]. On the other hand, Fe-Pani-RGO 2 py gains a large positive effect in terms of onset and half-wave potential from 0.63 V to 0.82 V vs RHE and from 0.3 V to 0.74 V vs RHE, respectively ($\Delta E_{onset} = 0.19$ V vs RHE and $\Delta E_{½} = 0.37$ V vs RHE). Moreover, other samples show slightly increased half-wave potentials, i.e. Fe-Ammonia-RGO 2 py and Fe-ChoCl-RGO 2 py by 0.04 and 0.02 V, respectively. Obviously, Fe-Urea-RGO 2 py showed decrease in ORR activity after two-step pyrolysis, which negatively shifts the onset potential (ΔE_{onset}) by 0.16 V vs RHE and the half-wave by 0.45 V.

The mass transport-free region, as presented by the limiting current density, is a crucial part in describing the effect of step pyrolysis. Furthermore, it is consistent with the CV activity described above. As seen from Fig. 4(b & c) and Table 3, in the high overpotential region (0.2–0.4 V), most one-step pyrolysis catalysts show the absence of a limiting plateau in their current density, which can be linked to a dense aggregation on the surface and the dissolution of the iron phase that would hinder mass transport on the catalyst [36,76]. Interestingly, upon two-step pyrolysis, Fe-Pani-RGO 2 py achieves a limiting current density of up to 5.33 mA cm^{-2}, while Fe-ChoCl-RGO 2 py and Fe-Ammonia-RGO 2 py increase to values of 2.32 and 2.5 mA cm^{-2}, respectively. The limiting plateau of both N sources will be smaller than that of Pani owing to the existence of α-Fe_2O_3 that can be easily oxidized under acidic conditions. Thus, it is less favourable than the Fe-N_x moiety [77]. Fe-Urea-RGO 1 py also has a poor limiting plateau due to more oxygenated species of the iron phase from α-Fe_2O_3 into Fe_3O_4, that likely turning the mechanism into a two-electron pathway [77]. Two-step pyrolysis essentially increases the electron transfer of the catalyst via a highly ordered graphitic carbon structure [78]. This is in line with the FESEM morphology displaying the ordered thin sheet structure. The XRD pattern also show prominent peaks and graphitisation degrees after the second pyrolysis, as shown by the Raman spectroscopy. The high graphitic sites will further increase the mass transport during ORR activity [14,58].

As described in the above, Fe-Pani-RGO 2 py shows remarkable ORR activity under acidic conditions. The ORR activity is also comparable to that of the benchmark 10 wt.%

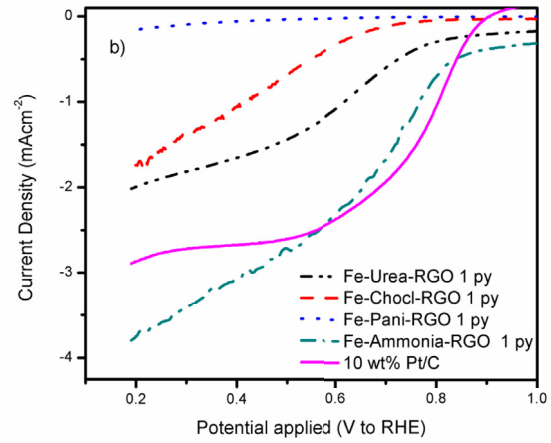

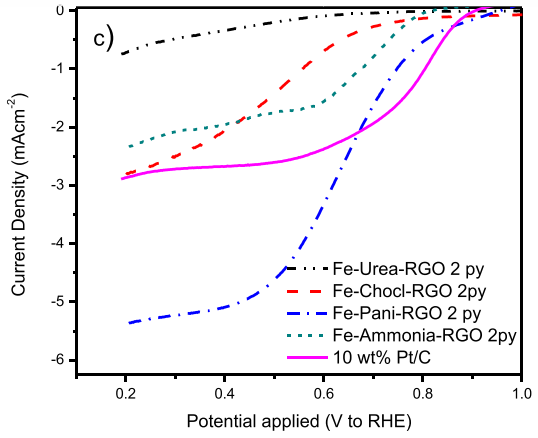

Fig. 4 – (*continued*).

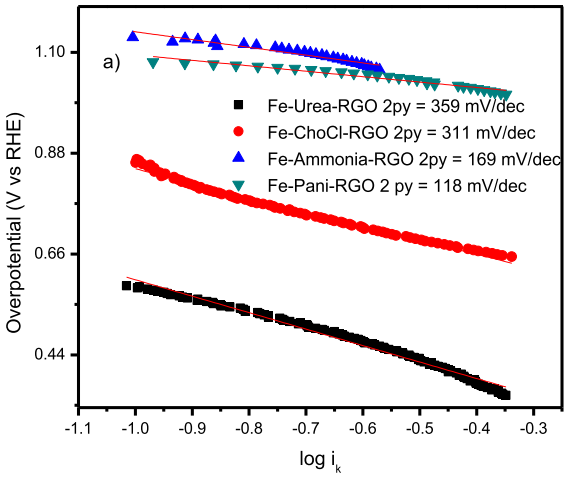

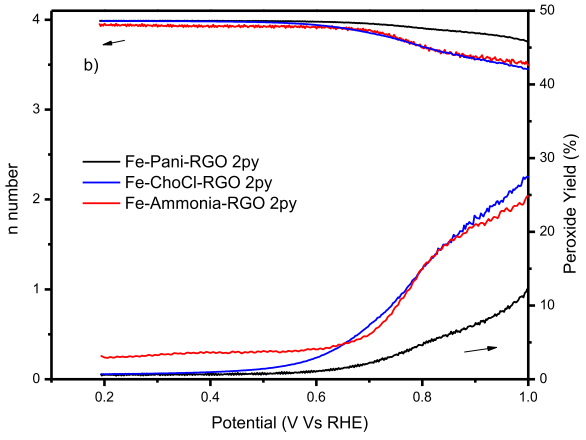

Fig. 5 – a) Tafel plot, b) *n* number and peroxide yield (%) for two-step pyrolysis. c) LSV curve in a range of 200–1600 rpm and the d) K-L plot of Fe-Pani-RGO 2 py.

Table 3 – Onset potential (E_{onset}), half-wave potential ($E_{1/2}$), current density (I) and electron transfer number (n) for ORR of Fe–N-RGO samples through one-step and two-step pyrolysis.

Samples	E_{onset} (V vs RHE)	$E_{1/2}$ (V vs RHE)	I (mA cm^{-2})	*n*
Fe-Urea-RGO 1 py	0.82	0.67	–	2.37
Fe-ChoCl-RGO 1 py	0.75	0.49	–	2.31
Fe-Pani-RGO 1 py	0.63	0.37	–	1.27
Fe-Ammonia-RGO 1 py	0.83	0.73	–	3.76
Fe-Urea-RGO 2 py	0.66	0.29	–	2.39
Fe-ChoCl-RGO 2 py	0.75	0.51	2.42	3.73
Fe-Pani-RGO 2 py	0.82	0.74	5.33	3.90
Fe-Ammonia-RGO 2 py	0.83	0.69	2.5	3.77
Fe-Pani-RGO Gr 2 py	0.71	0.54	1.17	2.3
Pt/C	0.93	0.79	3.05	3.99

Pt/C catalyst in terms of the onset potential (0.91 V for Pt/C) and half-wave potential difference (50 mV for Pt/C). On the aspect of active sites, Fe-Pani-RGO 2 py is greatly influenced by the major content of graphitic N (5.04 at.%) and the Fe-Nx moiety, which can decrease the activation barrier during ORR activity [79]. Additionally, the high surface area and pore volume of the porous surface should also improve the reactant pathway during the ORR [80].

Microkinetic analyses, such as Tafel plots and electron transfer number, were further conducted. As depicted in Fig. 5(a), the Tafel slope is measured at 25 °C in the mixed kinetic-diffusion region (1.0–0.6 V vs RHE) to determine the mechanism of electron and mass transfer in the kinetic region of the catalyst surface [81]. Among all samples, Fa-Pani-RGO 2 py displays the lowest Tafel slope value of 118 mV/dec, indicating a two-electron transfer as the rate determining step. These results showed superior ORR kinetics than that of the work done by Guo et al. [82], who prepared bimetallic FeCo-Pani-CNT with a self-molecular assembly method; the above catalyst resulted in a Tafel slope of 216 mV/dec under acidic conditions. In these regions, the surface catalyst produces a large number of peroxide molecules as a by-product and demonstrates slow kinetics when converting them into water molecules [8]. The other prepared samples display much higher Tafel slopes than Fe-Pani-RGO 2 py, which shows inferior ORR activity and is in good agreement with the earlier discussion. It is also worth noting that, with the highest slope

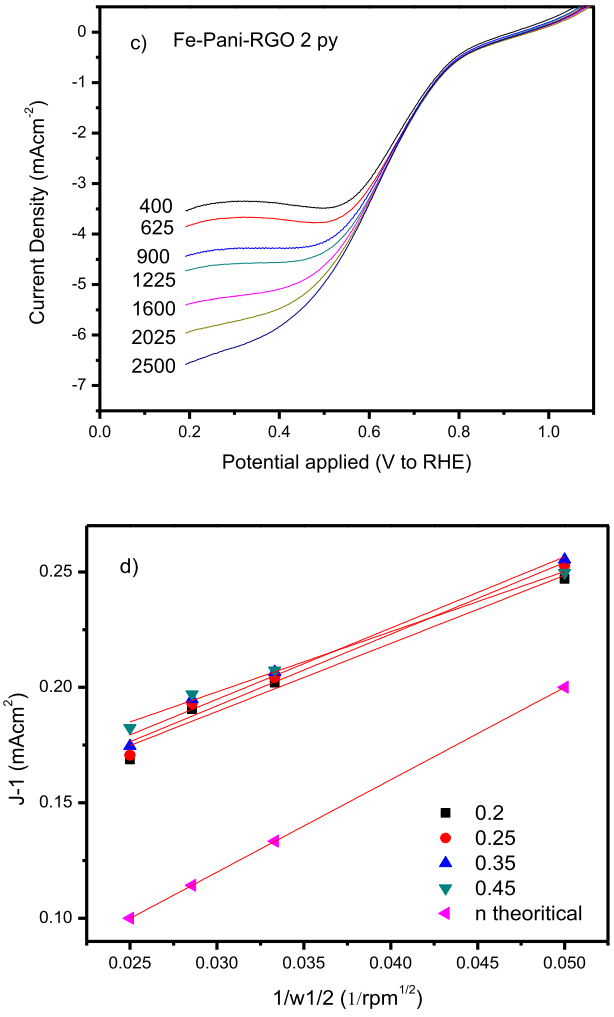

Fig. 5 – (*continued*).

obtained on Fe-Urea-RGO 2 py at 359 mV/dec, it shows the absence of a limiting current plateau, thus reflecting its very poor ORR activity. The low content of nitrogen sources, especially graphitic-N composition [83], high resistance and coarse structure of the catalyst inhibits the oxygen dissociation monolayer, thus leading to poor kinetic activity [84].

Moreover, the electron transfer number, *n*, was also calculated based on the current density on the disk and ring through the RRDE measurements. As seen from Fig. 5(b) and Table 2, Fe-Pani-RGO 2 py depicts $n = 3.90$, whereas Fe-ChoCl-RGO 2 py and Fe-Ammonia-RGO 2 py achieve *n* values of 3.73 and 3.77, respectively. These values infer a predominance for a four-electron transfer pathway to completely reduce the oxygen to water. In contrast, the *n* value obtained for Fe-Urea-RGO 2 py is 2.39, which shows a predominance for a two-electron transfer pathway to reduce oxygen to hydrogen peroxide, indicating its poor ORR kinetics and unsuitability as a catalyst. It is worth noting that the peroxide yield from the platinum ring detection is calculated as approximately 10% for Fe-Pani-RGO 2py, while another catalyst produces a large peroxide yield of approximately 25%. Fig. 5(c) and d further demonstrate the LSV and the extracted data into the K-L plot of Fe-Pani-RGO 2 py, which shows a proportional change between the rotation speed and current density with an apparent current limiting plateau [85]. This implies that two-step pyrolysis, especially for the Fe-Pani-RGO 2 py, has successfully tuned the catalyst to possess the desirable active sites and graphitic properties for improving the ORR kinetics in acidic environments.

Kinetic analysis, durability and methanol tolerance of Fe-pani-RGO 2 py

A temperature dependence study for ORR activity was tested in an attempt to simulate the catalyst under actual electrode conditions. Thus, the kinetic parameter for the ORR is interpreted from the polarisation curve obtained for the Fe-Pani-RGO 2 py sample with a temperature increase from 25 to 80 °C. As depicted in Fig. 6(a–c) in the kinetic region, both the onset and half-wave potentials increase with increasing half-cell temperature. It is also calculated that the Tafel slope obtained in the kinetic region shows a decrease from 118 $mVdec^{-1}$ to 74 mV/dec, achieving a value near that of the Pt/C slope (60 $mVdec^{-1}$); the above results indicate a low energy barrier for the reaction at 80 °C, which is beneficial for the actual PEMFC environment. Moreover, a similar trend also occurs in the high overpotential region, achieving a Tafel slope close to that for Pt/C (120 mV/dec); notably, a reduction in intermediate OH * coverage accelerates the kinetics of mass transfer [86,87]. The exchange current density calculated in the above temperature range for Fe-Pani-RGO 2 py varies between 7.47 10^{-6}-1.03 $\times$ 10^{-6} mA cm^{-2} with a transfer constant, $\alpha = 0.29–0.53$. The value is one order of magnitude higher than that of the Pt alloys (PtFe/C = 2.15 $\times$ 10^{-7} mA cm^{-2}), thus indicating a higher intrinsic of catalytic activity [87].

To ensure the long-term operability of the catalyst, the stability of iron metal-doped with carbon sources were reported. Therefore, a half-cell simulation was conducted via a chronoamperometry test in the cathode environment. For the LSV curve, the potential applied to the electrode was constantly kept at the Fe-Pani-RGO 2 py diffusion region (0.25 V). After 16,000 s of running at 1600 rpm in a saturated O_2 and acidic environment, Fe-Pani-RGO retains a current density 8% higher than that of the benchmark Pt/C (Fig. 7(a)). This highlights that even the current density of Fe-Pani-RGO 2 py is slightly lower than that of the benchmark Pt/C, but its durability over extended use should be considered. The thin layer and rich mesoporous morphology and the synergistic effect of the iron-nitrogen active sites (Fe-N_x site) has created a stable carbon matrix that is able to prevent catalyst degradation during the oxygen reduction process [88]. The methanol tolerance of Fe-Pani-RGO 2 py is 20% higher than Pt/C (Fig. 7(b)) after adding 3 mol/mL methanol for 1200 s. It can be noted that the catalyst has the capability to prevent carbon poisoning and metal dissolution under methanol conditions [89].

Comparison to RGO graphite and other catalysts

Based on the above characteristics, the two-step pyrolysis with Pani (Fe-Pani-RGO 2py) demonstrates the highest ORR activity and stability. Thus, comparisons to commercial RGO from graphite are made by preparing Fe-Pani-RGO Gr with

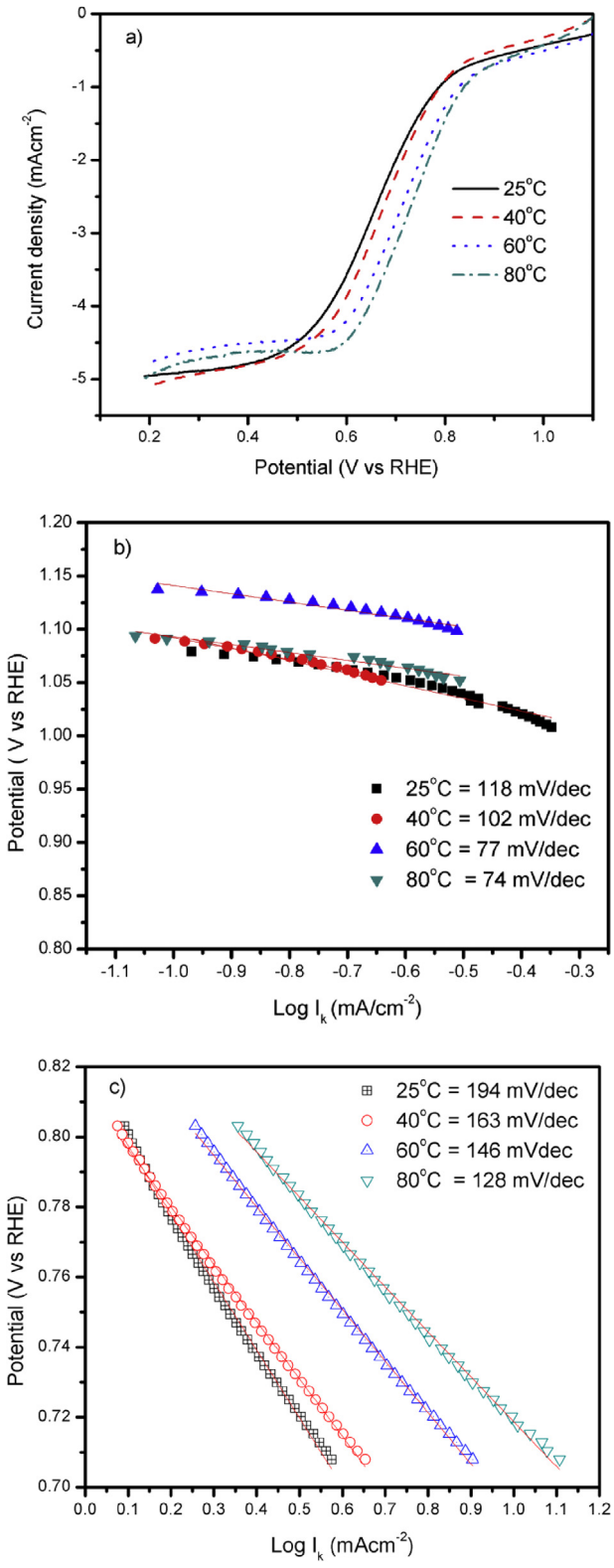

Fig. 6 – Temperature dependence of the Fe-Pani-RGO 2 py a) LSV curve; tafel plot at b) low current density and c) high current density.

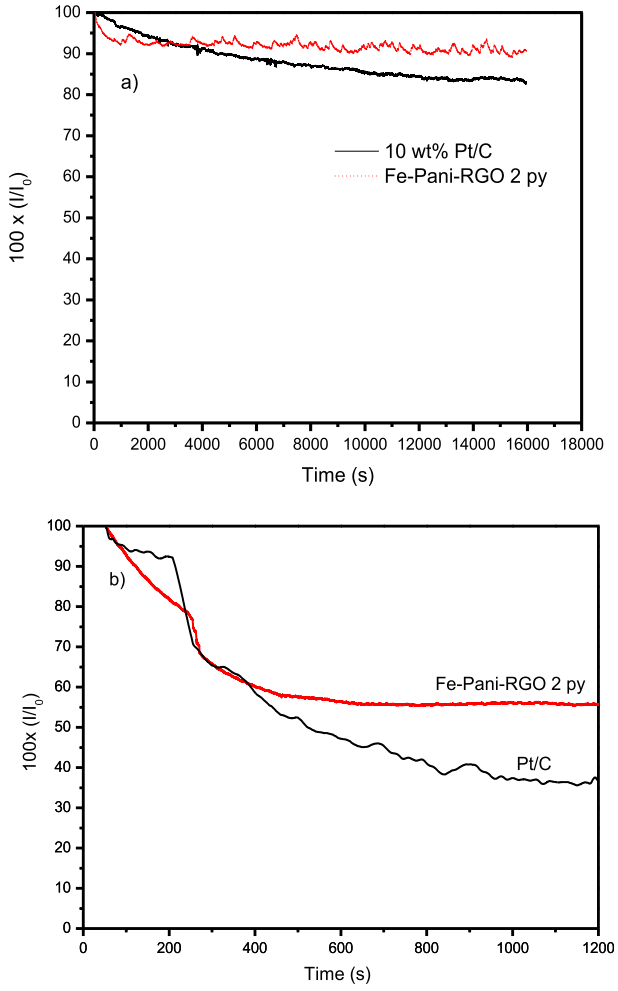

Fig. 7 – Chronoamperometry (CA) test at 1600 rpm in saturated O_2 environment with 0.1 M $HClO_4$: a) the stability during 16,000 s and the b) methanol tolerance during 1200 s for Fe-Pani-RGO 2 py and Pt/C.

two-step pyrolysis. Both catalysts are compared based on Cyclic Voltammetry (CV) tests to determine the catalytic performance under static mass transfer. As mentioned in Fig. S6, the redox reaction of the iron state in Fe-Pani-RGO 2 py resembles that of consecutive Fe-Pani-RGO Gr. This implies an analogue surface condition, which also corresponds to the chemical state and crystallinity characterization. X-ray diffraction shows carbon peaks at $2\theta = 26°$ and a peak at $2\theta = 44°$ for iron carbide (see Fig. S7) Moreover, the XPS results demonstrate an overall Fe content of 3.23 at.% and a N content of 10.33 at.%, which are slightly lower than those of Fe-Pani-RGO 2 py (refer to Table S2).

It is obvious that the ORR activity of Fe-Pani-RGO Gr shows a negative shift in onset potential up to 0.71 V, and the half wave potential is 0.54 V (refer to Fig. S8). In a potential range similar to Fe-Pani-RGO 2py, the current density in the diffusion region (high potential, < 0.5 V vs RHE) did not yet reach the limiting plateau. It is worth noting that the type of chemical bonding, morphology and porous structure affects the activity. The XPS spectra depicts higher amount of pyridinic N (4.23 at.%) on Fe-Pani-RGO Gr instead of the graphitic N found in Fe-Pani-RGO 2py. Under acidic conditions, an increase in proton absorption in pyridinic N occurs and thereby initiates a major production of peroxide that decreases the

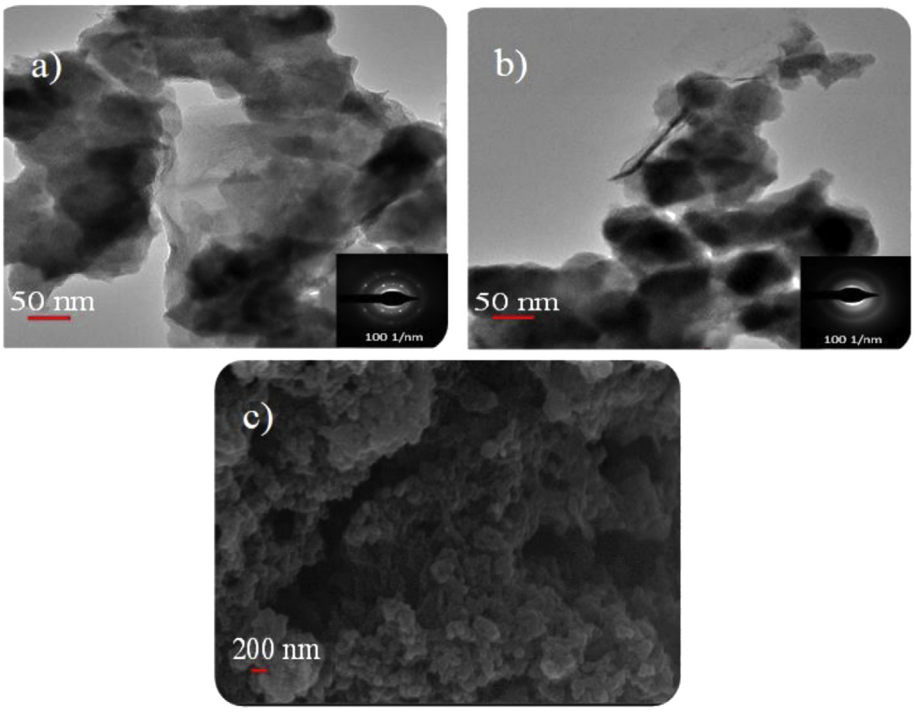

Fig. 8 – TEM of (a–b) Fe-Pani-RGO 2 py and Fe-Pani-RGO Gr and the c) FESEM of Fe-Pani-RGO Gr.

ORR activity [86]. As seen in Fig. 8(a–c) the morphology from the FESEM and TEM analyses further explain the low activity of Fe-Pani-RGO Gr in an acidic medium compare to Fe-Pani RGO 2 py. Agglomerated and condensed structures on Fe-Pani-RGO Gr are observed on the surface, which may lead to the blockage of active sites. In conjunction with the XPS results, the number of N oxides and the total oxygen content in Fe-Pani-RGO Gr have adverse effects on the ORR activity. A high oxygen content was resulted from the unsuccessful reduction of oxygen in the GO layer, thus affecting the self-wrinkling behaviour and the amorphous sites of the graphene oxide layer and Pani. Furthermore, there is a decrease in metallic iron that occurs since RGO Gr has a large number of macropores and oxidative activity [90].

From the SAED analysis, the diffraction ring observed on Fe-Pani-RGO Gr also implies an amorphous crystal structure on the catalyst compared to the diffraction spot that is observed with Fe-Pani-RGO 2 py. The amorphous structure also agrees with the XRD result, which shows less prominent peaks on Fe-Pani-RGO Gr (refer to Fig. S8). As reported in Table 1, the two catalysts Fe-Pani-RGO Gr and Fe-Pani-RGO 2 py have similar surface areas ranging from 18.9 to 29.2 m^2g^{-1}, respectively. It is worth noting that the specific surface area of the Fe-Pani-RGO 2 py in this work was found lower than other Fe-Pani based catalyst from literature, i.e.: Fe-Pani-CNC and Fe-Pani/CNT with surface area up to 398 m^2g^{-1} [91] and 354 m^2g^{-1} [83], respectively. This is possibly due to the presence of bulky unexfoliated structure on the internal part of the biomass RGO. It can also be attributed to the lower exfoliation degree that led to the restacking of the carbon layer in the biomass RGO. Nonetheless, the current density obtained by the Fe-Pani-RGO 2 py (5.33 $mAcm^{-2}$) in this work was found comparable with Fe-Pani-CNC (5 mA/cm^{-2}) reported by Tang et.al. While pore examination via BJH adsorption has indicated that the Fe-Pani-RGO 2 py catalyst exhibited an evenly distributed mesopores (21.2 nm), similar to that with his work on Fe-Pani-CNC reported the values of 20–50 nm [91] despite much lower specific surface area in our work. Hence, we deduce that mass transport on catalyst may not be solely dependent on the higher surface area but affected by other factors such as pore volume and pore size distribution [92]. The mesoporous structure with multilayer porous network possessed in the RGO derived from Sengon wood support maybe the unique characteristic that was able to prevent carbon corrosion that hinders the loss of Fe-N_x moiety and graphitic N under acidic conditions that could improve the durability of the catalyst as shown in Fig. 7(a) [58,90].

In addition to ensure the remarkable ORR activity of Fe-Pani-RGO 2 py, the work are also compares to other structure Fe–N–C catalyst was reported by Videla et al. [18] in which they incorporated iron salt, polymeric salt (TPTZ) and

Table 4 – Comparison of the ORR activity through E_{onset} and n of Fe-Pani-RGO 2 py with literature works.

Catalyst	E_{onset} (V vs RHE)	*n*	References
Fe-Phen-C 900	0.82	4.0	[74]
Fe-Bipyr/C	0.71	3.3	[93]
Fe-Pani-Mela/C	0.98	4	[94]
Fe-Pani-CNC	0.75	–	[91]
Fe-Pani-RGO 2 py	0.83	3.90	This work

RGO into a Fe–N–C catalyst with a limiting current density of 3.5 mA cm^{-2} and an onset potential of 0.8 V (vs RHE) in 0.5 M H_2SO_4. Table 4 shows that the result of our work is comparable to previous research in acidic environments. The ORR result may be lower than existing work, but from the perspective of availability and cost issues, this catalyst is promising.

Conclusion

Two-step pyrolysis has successfully tuned the distribution of iron and nitrogen into the RGO lattice, increased the degree of graphitisation and generated more stabilized graphitic N bonds, which are believed to be the major contributors in improving the ORR activity and the stability of the Fe–N-RGO catalyst. The mesoporous structure of the RGO support derived from Sengon wood was able to retain iron metal and nitrogen and exhibited stable ORR activity, retaining 92% of its current density after 16,000 s under acidic conditions. The highest ORR activity was achieved by Fe-Pani-RGO 2 py with an onset potential of 0.84 V, a current density of 5.33 mA cm^{-2} and a half-wave potential difference ($\Delta E_{1/2}$) of 50 mV comparable to that of Pt/C. This catalyst also showed an approximately 20% higher methanol tolerance than Pt/C. These results revealed the potential of producing natural biomass RGO as a sustainable noble-metal-free catalyst support for high ORR activity. Further work to gain better insight into the applicability of RGO derived from sengon wood would be focus on optimising the elemental composition and control the pore structure of the Fe-Pani-RGO 2py catalyst that would be able to applied in PEMFC for longer and stable operation.

Declaration of competing interest

The authors declare that they have no known competing financial interests or personal relationships that could have appeared to influence the work reported in this paper.

Acknowledgement

The authors would like to acknowledge the financial support from the Fundamental Research Grant Scheme (FRGS/1/2019/STG01/UKM/02/2) by the Ministry of Education Malaysia and Universiti Kebangsaan Malaysia through the project GUP-2018-013. The authors would also like to thank Nuclear Malaysia for providing the FESEM, Raman and XRD facilities for the characterizations, the Synchotron Light Research Institute (SLRI) Thailand for providing XPS characterization, and the Center of Research and Instrumentation (CRIM) UKM for the TEM analysis.

Appendix A. Supplementary data

Supplementary data to this article can be found online at https://doi.org/10.1016/j.ijhydene.2020.05.158.

REFERENCES

[1] Shao M, Chang Q, Dodelet J-P, Chenitz R. Recent advances in electrocatalysts for oxygen reduction reaction. Chem Rev 2016;116:3594–657. https://doi.org/10.1021/acs.chemrev.5b00462.

[2] Jiang K, Zhang X, Huang J, Wang S, Chen J. Porous hollow tubular carbon materials based on zeolitic imidazolate framework-8 derived from ZnO nanorods as new enzyme immobilizing matrix for high-performance bioanode of glucose/O_2biofuel cells. J Electroanal Chem 2017;796:88–95. https://doi.org/10.1016/j.jelechem.2017.04.054.

[3] Yahya N, Kamarudin SK, Karim NA, Basri S, Zanoodin AM. Nanostructured Pd-based electrocatalyst and membrane electrode assembly behavior in a passive direct glycerol fuel cell. Nanoscale Res Lett 2019;14. https://doi.org/10.1186/s11671-019-2871-8.

[4] Chumillas S, Maestro B, Feliu JM, Climent V. Comprehensive study of the enzymatic catalysis of the electrochemical oxygen reduction reaction (ORR) by immobilized copper efflux oxidase (CueO) from Escherichia coli. Front Chem 2018;6:1–16. https://doi.org/10.3389/fchem.2018.00358.

[5] Vats T, Dutt S, Kumar R, Siril PF. Facile synthesis of pristine graphene-palladium nanocomposites with extraordinary catalytic activities using swollen liquid crystals. Sci Rep 2016;6:1–11. https://doi.org/10.1038/srep33053.

[6] Shi J, Wang Y, Du W, Hou Z. Synthesis of graphene encapsulated Fe_3C in carbon nanotubes from biomass and its catalysis application. Carbon N Y 2016;99:330–7. https://doi.org/10.1016/j.carbon.2015.12.049.

[7] Gewirth AA, Varnell JA, Diascro AM. Nonprecious metal catalysts for oxygen reduction in heterogeneous aqueous systems. Chem Rev 2018;118:2313–39. https://doi.org/10.1021/acs.chemrev.7b00335.

[8] Zhang X, Lu P, Zhang C, Cui X, Xu Y, Qu H, et al. Towards understanding ORR activity and electron-transfer pathway of M-Nx/C electro-catalyst in acidic media. J Catal 2017;356:229–36. https://doi.org/10.1016/j.jcat.2017.10.020.

[9] Bezerra CWB, Zhang L, Lee K, Liu H, Marques ALB, Marques EP, et al. A review of Fe-N/C and Co-N/C catalysts for the oxygen reduction reaction. Electrochim Acta 2008;53:4937–51. https://doi.org/10.1016/j.electacta.2008.02.012.

[10] Jiang W-J, Gu L, Li L, Zhang Y, Zhang X, Zhang L-J, et al. Understanding the high activity of Fe–N–C electrocatalysts in oxygen reduction: Fe/Fe_3 C nanoparticles boost the activity of Fe–Nx. J Am Chem Soc 2016;138:3570–8. https://doi.org/10.1021/jacs.6b00757.

[11] Zheng Y, Yang DS, Kweun JM, Li C, Tan K, Kong F, et al. Rational design of common transition metal-nitrogen-carbon catalysts for oxygen reduction reaction in fuel cells. Nanomater Energy 2016;30:443–9. https://doi.org/10.1016/j.nanoen.2016.10.037.

[12] Chen X, Ge F, Chang J, Lai N. Exploring the catalytic activity of metal-fullerene C 58 M (M = Mn, Fe, Co, Ni, and Cu) toward oxygen reduction and CO oxidation by density functional theory. Int J Energy Res 2019:1–9. https://doi.org/10.1002/er.4768.

[13] Osmieri L, Escudero-Cid R, Armandi M, Monteverde Videla AHA, García Fierro JL, Ocón P, et al. Fe-N/C catalysts for oxygen reduction reaction supported on different carbonaceous materials. Performance in acidic and alkaline direct alcohol fuel cells. Appl Catal B Environ 2017;205:637–53. https://doi.org/10.1016/j.apcatb.2017.01.003.

[14] Negro E, Videla AHAMM, Baglio V, Aricò AS, Specchia S, Koper GJM. Fe–N supported on graphitic carbon nano-

networks grown from cobalt as oxygen reduction catalysts for low-temperature fuel cells. Appl Catal B Environ 2015;166–167:75–83. https://doi.org/10.1016/j.apcatb.2014.10.074.
[15] Morales-Narváez E, Sgobbi LF, Machado SAS, Merkoçi A. Graphene-encapsulated materials: synthesis, applications and trends. Prog Mater Sci 2017;86:1–24. https://doi.org/10.1016/j.pmatsci.2017.01.001.
[16] Park HS, Han SB, Kwak DH, Han JH, Park KW. Fe nanoparticles encapsulated in doped graphitic shells as high-performance and stable catalysts for oxygen reduction reaction in an acid medium. J Catal 2019;370:130–7. https://doi.org/10.1016/j.jcat.2018.12.015.
[17] Wu G, More KL, Johnston CM, Zelenay P. High-performance electrocatalysts for oxygen reduction derived from polyaniline, iron, and cobalt. Science 2011;332:443–7. https://doi.org/10.1126/science.1200832. 80-.
[18] Monteverde Videla AHA, Ban S, Specchia S, Zhang L, Zhang J. Non-noble Fe-NX electrocatalysts supported on the reduced graphene oxide for oxygen reduction reaction. Carbon N Y 2014;76:386–400. https://doi.org/10.1016/j.carbon.2014.04.092.
[19] Kang S, Kim H, Chung Y-H. Recent developments of nano-structured materials as the catalysts for oxygen reduction reaction. Nano Converg 2018;5:13. https://doi.org/10.1186/s40580-018-0144-3.
[20] Liu GCK, Dahn JR. Fe-N-C oxygen reduction catalysts supported on vertically aligned carbon nanotubes. Appl Catal Gen 2008;347:43–9. https://doi.org/10.1016/j.apcata.2008.05.035.
[21] Ekhlasi L, Younesi H, Rashidi A, Bahramifar N. Populus wood biomass-derived graphene for high CO_2 capture at atmospheric pressure and estimated cost of production. Process Saf Environ Protect 2018;113:97–108. https://doi.org/10.1016/j.psep.2017.09.017.
[22] Guizani C, Jeguirim M, Valin S, Limousy L, Salvador S. Biomass chars: the effects of pyrolysis conditions on their morphology, structure, chemical properties and reactivity. Energies 2017;10(6):796. https://doi.org/10.3390/en10060796.
[23] Xia L, Wu X, Wang Y, Niu Z, Liu Q, Li T, et al. S-doped carbon nanospheres: an efficient electrocatalyst toward artificial N_2 fixation to NH3. Small Methods 2019;3:2–6. https://doi.org/10.1002/smtd.201800251.
[24] Meng H, Chen X, Gong T, Liu H, Liu Y, Li H, et al. N, P, S/Fe–codoped carbon derived from Feculae Bombycis as an efficient electrocatalyst for oxygen reduction reaction. ChemCatChem 2019;11(24):6015–21. https://doi.org/10.1002/cctc.201900604.
[25] Wang G, Peng H, Qiao X, Du L, Li X, Shu T, et al. Biomass-derived porous heteroatom-doped carbon spheres as a high-performance catalyst for the oxygen reduction reaction. Int J Hydrogen Energy 2016;41:14101–10. https://doi.org/10.1016/j.ijhydene.2016.06.023.
[26] Guo CZ, Liao WL, Chen CG. Design of a non-precious metal electrocatalyst for alkaline electrolyte oxygen reduction by using soybean biomass as the nitrogen source of electrocatalytically active center structures. J Power Sources 2014;269:841–7. https://doi.org/10.1016/j.jpowsour.2014.07.024.
[27] Sun Z, Zheng M, Hu H, Dong H, Liang Y, Xiao Y, et al. From biomass wastes to vertically aligned graphene nanosheet arrays: a catalyst-free synthetic strategy towards high-quality graphene for electrochemical energy storage. Chem Eng J 2018;336:550–61. https://doi.org/10.1016/j.cej.2017.12.019.
[28] Chen R, Huo J, Yan D, Dai L, Li Y, Wang S. Defect chemistry of nonprecious-metal electrocatalysts for oxygen reactions. Adv Mater 2017;29:1606459. https://doi.org/10.1002/adma.201606459.
[29] Cordeiro GL. Defect engineering in reduced graphene oxide toward advanced energy conversion. Intech; 2018. p. 93. https://doi.org/10.5772/57353.
[30] Zhao J, Wang B, Zhou Q, Wang H, Li X, Chen H, et al. Efficient electrohydrogenation of N_2 to NH_3 by oxidized carbon nanotubes under ambient conditions. Chem Commun 2019;55:4997–5000. https://doi.org/10.1039/c9cc00726a.
[31] Kačík F, Ďurkovič J, Kačíková D. Chemical profiles of wood components of poplar clones for their energy utilization. Energies 2012;5:5243–56. https://doi.org/10.3390/en5125243.
[32] Wulandhari Syarif N, Waruwu I, Prayogo MR. Sengon wood (Paraserianthes falcataria (L.) Nielsen) carbon as supporting material for electrochemical double layer capasitor. IOP Conf Ser Mater Sci Eng 2017;223. https://doi.org/10.1088/1757-899X/223/1/012047.
[33] Sudarsono W, Wong WY, Loh KS, Majlan EH, Syarif N, Kok K, et al. Noble-free oxygen reduction reaction catalyst supported on Sengon wood (Paraserianthes falcataria L.) derived reduced graphene oxide for fuel cell application. Int J Energy Res 2020;44:1761–74. https://doi.org/10.1002/er.5015.
[34] Samad S, Loh KS, Wong WY, Sudarsono W, Lee TK, Wan Daud WR. Effect of various Fe/Co ratios and annealing temperatures on a Fe/Co catalyst supported with nitrogen-doped reduced graphene oxide towards the oxygen reduction reaction. J Alloys Compd 2020;816:152573. https://doi.org/10.1016/j.jallcom.2019.152573.
[35] Zhao J, Liu Y, Quan X, Chen S, Yu H, Zhao H. Nitrogen-doped carbon with a high degree of graphitization derived from biomass as high-performance electrocatalyst for oxygen reduction reaction. Appl Surf Sci 2017;396:986–93. https://doi.org/10.1016/j.apsusc.2016.11.073.
[36] Gu L, Jiang L, Li X, Jin J, Wang J, Sun G. A Fe-N-C catalyst with highly dispersed iron in carbon for oxygen reduction reaction and its application in direct methanol fuel cells. Cuihua Xuebao/Chinese J Catal 2016;37:539–48. https://doi.org/10.1016/S1872-2067(15)61049-X.
[37] Elgrishi N, Rountree KJ, McCarthy BD, Rountree ES, Eisenhart TT, Dempsey JL. A practical beginner's guide to cyclic voltammetry. J Chem Educ 2018;95:197–206. https://doi.org/10.1021/acs.jchemed.7b00361.
[38] Xing W, Yin G, Zhang J. Rotating electrode methods and oxygen reduction electrocatalysts. 2014. https://doi.org/10.1016/C2012-0-06455-1.
[39] Tavakoli F, Salavati-Niasari M, Badiei A, Mohandes F. Green synthesis and characterization of graphene nanosheets. Mater Res Bull 2015;63:51–7. https://doi.org/10.1016/j.materresbull.2014.11.045.
[40] Khojasteh H, Salavati-Niasari M, Safajou H, Safardoust-Hojaghan H. Facile reduction of graphene using urea in solid phase and surface modification by N-doped graphene quantum dots for adsorption of organic dyes. Diam Relat Mater 2017;79:133–44. https://doi.org/10.1016/j.diamond.2017.09.011.
[41] Mahmud RA, Shafawi AN, Ahmed Ali K, Putri LK, Rosli Ni Md, Mohamed AR. Graphene nanoplatelets with low defect density as a synergetic adsorbent and electron sink for ZnO in the photocatalytic degradation of Methylene Blue under UV–vis irradiation. Mater Res Bull 2020;128:110876. https://doi.org/10.1016/j.materresbull.2020.110876.
[42] Shafawi AN, Mahmud RA, Ahmed Ali K, Putri LK, Rosli Ni Md, Mohamed AR. Bi_2O_3 particles decorated on porous g-C_3N_4 sheets: enhanced photocatalytic activity through a direct Z-scheme mechanism for degradation of Reactive Black 5 under UV–vis light. J Photochem Photobiol Chem 2020;389. https://doi.org/10.1016/j.jphotochem.2019.112289.

[43] Song MY, Park HY, Yang DS, Bhattacharjya D, Yu JS. Seaweed-derived heteroatom-doped highly porous carbon as an electrocatalyst for the oxygen reduction reaction. ChemSusChem 2014;7:1755–63. https://doi.org/10.1002/cssc.201400049.
[44] López-Salas N, Carriazo D, Gutiérrez MC, Ferrer ML, Ania CO, Rubio F, et al. Tailoring the textural properties of hierarchical porous carbons using deep eutectic solvents. J Mater Chem 2016;4:9146–59. https://doi.org/10.1039/c6ta02704k.
[45] Mondal D, Sharma M, Wang C-H, Lin Y-C, Huang H-C, Saha A, et al. Deep eutectic solvent promoted one step sustainable conversion of fresh seaweed biomass to functionalized graphene as a potential electrocatalyst. Green Chem 2016;18:2819–26. https://doi.org/10.1039/C5GC03106K.
[46] Singh K, Ohlan Anil, Pham Viet Hung, Balasubramaniyan R, Varshney Swati, Jang Jinhee, et al. Nanostructured graphene/Fe_3O_4 incorporated polyaniline as a high performance shield against electromagnetic pollution. Nanoscale 2013;5.
[47] Kang D, Liu Q, Gu J, Su Y, Zhang W, Zhang D. Egg-box Assisted fabrication of porous carbon with small mesopores for high-rate electric double layer capacitors. ACS Nano 2015;9:11225–33. https://doi.org/10.1021/acsnano.5b04821.
[48] Liu J, Yu S, Daio T, Ismail MS, Sasaki K, Lyth SM. Metal-free nitrogen-doped carbon foam electrocatalysts for the oxygen reduction reaction in acid solution. J Electrochem Soc 2016;163:F1049–54. https://doi.org/10.1149/2.0631609jes.
[49] Wu G, More KL, Xu P, Wang HL, Ferrandon M, Kropf AJ, et al. A carbon-nanotube-supported graphene-rich non-precious metal oxygen reduction catalyst with enhanced performance durability. Chem Commun 2013;49:3291–3. https://doi.org/10.1039/c3cc39121c.
[50] Guo D, Han S, Wang J, Zhu Y. MIL-100-Fe derived N-doped Fe/Fe_3C@C electrocatalysts for efficient oxygen reduction reaction. Appl Surf Sci 2018;434:1266–73. https://doi.org/10.1016/j.apsusc.2017.11.230.
[51] Mousavi MF, Hashemi M, Rahmanifar MS, Noori A. Synergistic effect between redox additive electrolyte and PANI-rGO nanocomposite electrode for high energy and high power supercapacitor. Electrochim Acta 2017;228:290–8. https://doi.org/10.1016/j.electacta.2017.01.027.
[52] Parsaee Z, Karachi N, Abrishamifar SM, Kahkha MRR, Razavi R. Silver-choline chloride modified graphene oxide: novel nano-bioelectrochemical sensor for celecoxib detection and CCD-RSM model. Ultrason Sonochem 2018;45:106–15. https://doi.org/10.1016/j.ultsonch.2018.03.009.
[53] Niu Y, Huang X, Hu W. Fe_3C nanoparticle decorated Fe/N doped graphene for efficient oxygen reduction reaction electrocatalysis. J Power Sources 2016;332:305–11. https://doi.org/10.1016/j.jpowsour.2016.09.130.
[54] Huang Y, Liu W, Kan S, Liu P, Hao R, Hu H, et al. Tuning morphology and structure of Fe–N–C catalyst for ultra-high oxygen reduction reaction activity. Int J Hydrogen Energy 2020;45:6380–90. https://doi.org/10.1016/j.ijhydene.2019.12.130.
[55] Tong J, Li Y, Bo L, Wang W, Li T, Zhang Q. Core-shell Fe_3O_4@NCS-Mn derived from chitosan-schiff based mn complex with enhanced catalytic activity for oxygen reduction reaction. Catalysts 2019;9. https://doi.org/10.3390/catal9080692.
[56] Lee J, Kwak SY. Mn-doped maghemite (γ-Fe_2O_3) from metal-organic framework accompanying redox reaction in a bimetallic system: the structural phase transitions and catalytic activity toward NO_x removal. ACS Omega 2018;3:2634–40. https://doi.org/10.1021/acsomega.7b01865.
[57] Liu M, Liu J, Song Y, Li Z, Wang F. Mononuclear iron-dependent electrocatalytic activity of metal-nitrogen-carbon catalysts for efficient oxygen reduction reaction. Appl Catal Gen 2019;583:117120. https://doi.org/10.1016/j.apcata.2019.117120.
[58] Ren G, Gao L, Teng C, Li Y, Yang H, Shui J, et al. Ancient chemistry "pharaoh's snakes" for efficient Fe-/N-doped carbon electrocatalysts. ACS Appl Mater Interfaces 2018;10:10778–85. https://doi.org/10.1021/acsami.7b16936.
[59] Artyushkova K, Matanovic I, Halevi B, Atanassov P. Oxygen binding to active sites of Fe-N-C ORR electrocatalysts observed by ambient-pressure XPS. J Phys Chem C 2017;121:2836–43. https://doi.org/10.1021/acs.jpcc.6b11721.
[60] Song MY, Park HY, Yang DS, Bhattacharjya D, Yu JS. Seaweed-derived heteroatom-doped highly porous carbon as an electrocatalyst for the oxygen reduction reaction. ChemSusChem 2014;7:1755–63. https://doi.org/10.1002/cssc.201400049.
[61] Rivera Gavidia LM, García G, Anaya D, Querejeta A, Alcaide F, Pastor E. Carbon-supported Pt-free catalysts with high specificity and activity toward the oxygen reduction reaction in acidic medium. Appl Catal B Environ 2016;184:12–9. https://doi.org/10.1016/j.apcatb.2015.11.021.
[62] Domínguez C, Pérez-Alonso FJ, Salam MA, Al-Thabaiti SA, Peña MA, García-García FJ, et al. Repercussion of the carbon matrix for the activity and stability of Fe/N/C electrocatalysts for the oxygen reduction reaction. Appl Catal B Environ 2016;183:185–96. https://doi.org/10.1016/j.apcatb.2015.10.043.
[63] García Á, Retuerto M, Dominguez C, Pascual L, Ferrer P, Gianolio D, et al. Fe doped porous triazine as efficient electrocatalysts for the oxygen reduction reaction in acid electrolyte. Appl Catal B Environ 2020;264:118507. https://doi.org/10.1016/j.apcatb.2019.118507.
[64] Liu L, Yang X, Lv C, Zhu A, Zhu X, Guo S, et al. Seaweed-derived route to Fe_2O_3 Hollow nanoparticles/N-doped graphene aerogels with high lithium ion storage performance. ACS Appl Mater Interfaces 2016;8:7047–53. https://doi.org/10.1021/acsami.5b12427.
[65] Huang H, Wei X, Gao S. Nitrogen-doped porous carbon derived from malachium aquaticum biomass as a highly efficient electrocatalyst for oxygen reduction reaction. Electrochim Acta 2016;220:427–35. https://doi.org/10.1016/j.electacta.2016.10.108.
[66] Liang W, Chen J, Liu Y, Chen S. Density-functional-Theory calculation analysis of active sites for four-electron reduction of O_2 on Fe/N-doped graphene. ACS Catal 2014;4:4170–7. https://doi.org/10.1021/cs501170a.
[67] Lai L, Potts JR, Zhan D, Wang L, Poh CK, Tang C, et al. Exploration of the active center structure of nitrogen-doped graphene-based catalysts for oxygen reduction reaction. Energy Environ Sci 2012;5:7936–42. https://doi.org/10.1039/c2ee21802j.
[68] Yang S, Mao X, Cao Z, Yin Y, Wang Z, Shi M, et al. Onion-derived N, S self-doped carbon materials as highly efficient metal-free electrocatalysts for the oxygen reduction reaction. Appl Surf Sci 2018;427:626–34. https://doi.org/10.1016/j.apsusc.2017.08.222.
[69] Sotomayor FJ, Cychosz KA, Thommes M. Characterization of micro/mesoporous materials by physisorption: concepts and case studies. Acc Mater Surf Res 2018;3:34–50.
[70] Liu J, Takeshi D, Orejon D, Sasaki K, Lyth SM. Defective nitrogen-doped graphene foam: a metal-free, non-precious electrocatalyst for the oxygen reduction reaction in acid. J Electrochem Soc 2014;161:F544–50. https://doi.org/10.1149/2.095404jes.
[71] Soo LT, Loh KS, Mohamad AB, Daud WRW, Wong WY. Synthesis of silver/nitrogen-doped reduced graphene oxide through a one-step thermal solid-state reaction for oxygen reduction in an alkaline medium. J Power Sources

2016;324:412–20. https://doi.org/10.1016/j.jpowsour.2016.05.106.
[72] Chen C, Zhang X, Zhou Z-Y, Yang X-D, Zhang X-S, Sun S-G. Highly active Fe, N co-doped graphene nanoribbon/carbon nanotube composite catalyst for oxygen reduction reaction. Electrochim Acta 2016;222:1922–30. https://doi.org/10.1016/j.electacta.2016.12.005.
[73] Sharma R, Kar KK. Effects of surface roughness and N-content on oxygen reduction reaction activity for the carbon-based catalyst derived from poultry featherfiber. Electrochim Acta 2016;191:876–86. https://doi.org/10.1016/j.electacta.2016.01.166.
[74] Li L, Shen S, Wei G, Li X, Yang K, Feng Q, et al. A comprehensive investigation on pyrolyzed Fe-N-C composites as highly efficient electrocatalyst toward the oxygen reduction reaction of PEMFCs. ACS Appl Mater Interfaces 2019;11:14126–35. https://doi.org/10.1021/acsami.8b22494.
[75] Inagaki M, Toyoda M, Soneda Y, Morishita T. Nitrogen-doped carbon materials. Carbon N Y 2018;132:104–40. https://doi.org/10.1016/j.carbon.2018.02.024.
[76] Chen S, Niu Z, Xie C, Gao M, Lai M, Li M, et al. Effects of catalyst processing on the activity and stability of Pt-Ni nanoframe electrocatalysts. ACS Nano 2018;12:8697–705. https://doi.org/10.1021/acsnano.8b04674.
[77] Li J, Jia Q, Mukerjee S, Sougrati MT, Drazic G, Zitolo A, et al. The challenge of achieving a high density of Fe-based active sites in a highly graphitic carbon matrix. Catalysts 2019;9. https://doi.org/10.3390/catal9020144.
[78] Liu Y, Ruan J, Sang S, Zhou Z, Wu Q. Iron and nitrogen co-doped carbon derived from soybeans as efficient electrocatalysts for the oxygen reduction reaction. Electrochim Acta 2016;215:388–97. https://doi.org/10.1016/j.electacta.2016.08.090.
[79] Yan Y, Yan S, Yu Z, Zou Z. Low-work-function silver activating N-doped graphene as efficient oxygen reduction catalysts in acidic medium. ChemCatChem 2018;11. https://doi.org/10.1002/cctc.201801869. cctc.201801869.
[80] Ma Y, Luo S, Tian M, Lu JE, Peng Y, Desmond C, et al. Hollow carbon spheres codoped with nitrogen and iron as effective electrocatalysts for oxygen reduction reaction. J Power Sources 2020;450:227659. https://doi.org/10.1016/j.jpowsour.2019.227659.
[81] Wong WY, Daud WRW, Mohamad AB, Loh KS. Effect of temperature on the oxygen reduction reaction kinetic at nitrogen-doped carbon nanotubes for fuel cell cathode. Int J Hydrogen Energy 2015;40:11444–50. https://doi.org/10.1016/j.ijhydene.2015.06.006.
[82] Guo JW, Hu TH, Guo K, Wang JL. To pursue FexCoy-PANI/CNT catalysts for oxygen reduction reaction in acid medium with controlled molecular self-assembly method. Int J Hydrogen Energy 2018. https://doi.org/10.1016/j.ijhydene.2018.10.156. In press.
[83] Shi K-M, Cheng X, Jia Z-Y, Guo J-W, Wang C, Wang J. Oxygen reduction reaction of Fe-Polyaniline/Carbon Nanotube and Pt/C catalysts in alkali media. Int J Hydrogen Energy 2016;41:16903–12. https://doi.org/10.1016/j.ijhydene.2016.06.244.
[84] Rauf M, Zhao Y Di, Wang YC, Zheng YP, Chen C, Yang XD, et al. Insight into the different ORR catalytic activity of Fe/N/C between acidic and alkaline media: protonation of pyridinic nitrogen. Electrochem Commun 2016;73:71–4. https://doi.org/10.1016/j.elecom.2016.10.016.
[85] Sun T, Yang M, Chen H, Liu Y, Li H. N-doped and N/Fe-codoped porous carbon spheres derived from tetrazine-based polypyrrole as efficient electrocatalysts for the oxygen reduction reaction. Appl Catal Gen 2018;559:102–11. https://doi.org/10.1016/j.apcata.2018.04.028.
[86] Xue L, Li Y, Liu X, Liu Q, Shang J, Duan H, et al. Zigzag carbon as efficient and stable oxygen reduction electrocatalyst for proton exchange membrane fuel cells. Nat Commun 2018;9:2–9. https://doi.org/10.1038/s41467-018-06279-x.
[87] Song C, Zhang J. Electrocatalytic oxygen reduction reaction. PEM Fuel Cell Electrocatal. Catal. Layers Fundam. Appl. 2008:89–134. https://doi.org/10.1007/978-1-84800-936-3_2.
[88] Wang S, Zhu M, Bao X, Wang J, Chen C, Li H, et al. Synthesis of mesoporous Fe N/C materials with high catalytic performance in the oxygen reduction reaction. ChemCatChem 2015;7:2937–44. https://doi.org/10.1002/cctc.201500293.
[89] Yan Z, Dai C, Lv X, Zhang M, Zhao X, Xie J. Iron promoted nitrogen doped porous graphite for efficient oxygen reduction reaction in alkaline and acidic media. J Alloys Compd 2019;773:819–27. https://doi.org/10.1016/j.jallcom.2018.09.275.
[90] Ratso S, Käärik M, Kook M, Paiste P, Aruväli J, Vlassov S, et al. High performance catalysts based on Fe/N co-doped carbide-derived carbon and carbon nanotube composites for oxygen reduction reaction in acid media. Int J Hydrogen Energy 2019;44:12636–48. https://doi.org/10.1016/j.ijhydene.2018.11.080.
[91] Tang Shuihua, Huangfu Haixin, Dai Zhen, Leping Sui ZZ. Preparation of Fe-N-carbon nanocoils as catalyst for oxygen reduction reaction. Int J Electrochem Sci 2015;10:7180–91. https://doi.org/10.1111/ijcp.12507.
[92] Yu F, Wang C, Ma J. Capacitance-enhanced 3D graphene anode for microbial fuel cell with long-time electricity generation stability. Electrochim Acta 2018;259:1059–67. https://doi.org/10.1016/j.electacta.2017.11.038.
[93] Jäger R, Kasatkin PE, Härk E, Teppor P, Romann T, Härmas R, et al. The effect of N precursors in Fe-N/C type catalysts based on activated silicon carbide derived carbon for oxygen reduction activity at various pH values. J Electroanal Chem 2018;823:593–600. https://doi.org/10.1016/j.jelechem.2018.06.040.
[94] Peng H, Mo Z, Liao S, Liang H, Yang L, Luo F, et al. High performance Fe- and N- doped carbon catalyst with graphene structure for oxygen reduction. Sci Rep 2013;3:1765. https://doi.org/10.1038/srep01765.